Brain X chromosome inactivation is not random and can protect from paternally inherited neurodevelopmental disease.

Eric R Szelenyi[1,2,3], Danielle Fisenne[1,4,5], Joseph E Knox[6,7], Julie A Harris[6,8], James A Gornet[1,9,10], Ramesh Palaniswamy[1], Yongsoo Kim[1,11], Kannan Umadevi Venkataraju[1] and Pavel Osten[1]*

[1]Cold Spring Harbor Laboratory, Cold Spring Harbor, NY 11724.
[2]Program in Neuroscience, Stony Brook University, Neurobiology and Behavior, Stony Brook, NY 11794.
[3]Current address: University of Washington, Department of Biological Structure, Seattle, WA 98195
[4]Hofstra University, Hempstead, NY 11549.
[5]Certerra Inc., Farmingdale, NY 11735
[6]Allen Institute for Brain Science, Seattle, WA 98109
[7]Current address: Facebook, Seattle, WA 98109
[8]Current address: Cajal Neuroscience Inc, Seattle, WA 98102
[9]Columbia University, New York, NY 10027
[10]Current address: California Institute of Technology, Pasadena, CA 91125
[11]College of Medicine, Penn State University, Hershey, PA 17033
*Correspondence: osten@cshl.edu

Non-random (skewed) X chromosome inactivation (XCI) in the female brain can ameliorate X-linked phenotypes, though clinical studies typically consider 80-90% skewing favoring the healthy allele as necessary for this effect[1-10]. Here we quantify for the first time whole-brain XCI at single-cell resolution and discover a preferential inactivation of paternal to maternal X at ~60:40 ratio, which surprisingly impacts disease penetrance. In Fragile-X-syndrome mouse model, Fmr1-KO allele transmitted maternally in ~60% brain cells causes phenotypes, but paternal transmission in ~40% cells is unexpectedly tolerated. In the affected maternal Fmr1-KO(m)/+ mice, local XCI variability within distinct brain networks further determines sensory versus social manifestations, revealing a stochastic source of X-linked phenotypic diversity. Taken together, our data show that a modest ~60% bias favoring the healthy allele is sufficient to ameliorate X-linked phenotypic penetrance, suggesting that conclusions of many clinical XCI studies using the 80-90% threshold should be re-evaluated. Furthermore, the paternal origin of the XCI bias points to a novel evolutionary mechanism acting to counter the higher rate of *de novo* mutations in male germiline[11-16]. Finally, the brain capacity to tolerate a major genetic lesion in ~40% cells is also relevant for interpreting other neurodevelopmental genetic conditions, such as brain somatic mosaicism.

68 The X chromosome expresses more brain-specific genes than any other chromosome[17] and
69 X-linked gene mutations give rise to a high number of neurodevelopmental disorders,
70 including Rett syndrome (RTT), Fragile X syndrome (FXS) and more than one hundred
71 thirty X gene-linked intellectual disability and developmental disability disorders[17-23].

72 In female eutherian mammals, X chromosome inactivation (XCI) is thought to be
73 a random process by which either maternally inherited X (Xm) or paternally inherited X
74 (Xp) is chosen for epigenetic silencing, ensuring X dosage compensation compared to
75 males[24-27]. However, a non-random (skewed or biased) XCI pattern favoring one Xm or Xp
76 chromosome can occur as a consequence of a stochastic XCI fluctuation or developmental
77 selection against an X chromosome carrying a deleterious mutation. Such selection bias
78 favoring the healthy X chromosome has been proposed to occur in unaffected or only
79 mildly affected female carriers of X-linked brain disorders, with the degree of skewing
80 needed to reduce phenotypic penetrance typically defined as ≥80:20 selection ratio
81 favoring the healthy X[1-10]. The evidence for this model of XCI clinical significance,
82 however, remains inconclusive, as some studies reported correlations between
83 neurodevelopmental disease manifestations and XCI skewing measured in peripheral
84 blood cells, for example, in RTT and FXS[28-35], while others failed to identify consistent
85 evidence to support this[6,9,36-41], including three studies that directly examined XCI in
86 postmortem brains of RTT patients instead of relying on the indirect measure of XCI in
87 blood[6,9,36]. Therefore, the extent to which XCI skewing exists in normal female brain and,
88 even more importantly, the degree of skewing necessary to influence phenotypes in
89 heterozygous X-linked neurodevelopmental disorders remain unclear.

90 In the current study, we determined the degree to which X chromosome inactivation
91 (XCI) varies between individual female mice under normal conditions and the level of XCI
92 skewing that is necessary and sufficient to alter penetrance of X-linked
93 neurodevelopmental phenotypes in a mouse model of FXS. We applied our sensitive
94 methods of whole-brain imaging and computational data analyses[42-44] to reveal a novel XCI
95 pattern of ~60:40 bias favoring silencing of the paternal versus maternal X chromosome,
96 alongside a stochastic ~20% variability across all brain regions in each individual mouse.
97 Strikingly, this rather modest parent-of-origin bias and regional variability had clear effects
98 on phenotypic penetrance in the FXS mouse model. First, the overall paternal bias in XCI

99 protected offspring from the effects of the Fmr1-KO allele inherited from the father—a
100 finding that may represent a novel evolutionary mechanism countering the damaging
101 neurodevelopmental effects of a higher mutation rate in male germline line[11-16]. Second,
102 the local XCI fluctuations influenced the type of behavioral phenotype observed in mice
103 with Fmr1-KO allele inherited maternally—a result that suggests a novel stochastic source
104 of the broad phenotypic variability seen in X-linked neurodevelopmental disorders in
105 female patients and which can also help to localize different disease symptoms to candidate
106 affected brain regions, which may be useful in developing therapeutic strategies.
107

108 **Systematic parent-of-origin effect on brain XCI**

109 To obtain unbiased and complete survey of brain XCI we applied our serial two-photon
110 tomography (STPT)-based imaging and computational methods[42-44] to quantify maternal
111 versus paternal active X chromosome distribution using *knock-in* Mecp2-GFP reporter
112 mice[45-47] in which X-linked methyl-CpG-binding protein is tagged with GFP (Mecp2-GFP),
113 acting as a cellular reporter of the selection of the active X chromosome (Extended Data
114 Fig. 1-2).

115 We first compared the total number of brain cells with maternal X active in Mecp2-
116 GFP(m/+) mice that inherited the X-linked Mecp2-GFP allele maternally (n = 18) and the
117 total number of brain cells with paternal X active in Mecp2-GFP(p/+) mice that inherited
118 the Mecp2-GFP reporter allele paternally (n = 19). Surprisingly, this comparison revealed
119 significantly more GFP+ cells in the brains of the maternal Mecp2-GFP(m/+) mice,
120 demonstrating an average 58:42 bias towards higher paternal XCI and, consequently, an
121 average 58:42 ratio of cells with maternal Xm active to paternal Xp active in WT brain
122 (Fig. 1c, d; Supplementary Table 1). Notably, though, this average ~60:40 paternal XCI
123 bias comprised a considerable individual variability, including extreme examples of 84:16
124 Xm selection bias and 25:75 Xp selection bias (Fig. 1d). Therefore, stochastic variability
125 in XCI in early development, in addition to the systematic paternal bias, also plays an
126 important role in determining the overall Xm:Xp ratio in each brain (note that the Xm:Xp
127 ratios were calculated by normalizing the Mecp2-GFP(m/+) and Mecp2-GFP(p/+) cell
128 counts to the sum of Xm-active and Xp-active cell counts, which was equal to the 100%
129 control homozygous Mecp2-GFP(m/p) cell count; Fig. 1d; See Methods).

130 Next, we asked whether the paternal XCI bias seen at the whole-brain level exists
131 similarly across all brain areas or whether there may be regional differences in XCI patterns
132 in the brain. This analysis revealed that the average ~60:40 bias for maternal X selection is
133 seen across all major brain divisions, including the isocortex (58:42), cortical subplate
134 (58:42), olfactory areas (57:43), hippocampal formation (57:43), cerebral nuclei (57:43),
135 thalamus (58:42), hypothalamus (58:42), midbrain (60:40) and hindbrain (66:34) (Fig. 1e,
136 f; Supplementary Table 1, 2) as well as across all local subregions in these areas (Fig. 1g;
137 Supplementary Table 1, 2). These data thus argue against a previous model of cortical
138 versus subcortical differences in parent of origin XCI[48], suggesting instead that the
139 maternal X selection bias is seen not only in the cortex but also across the entire brain (note
140 that the anatomical segmentation of the imaged brains was done as previously described
141 by us using the 2011 ARA mouse brain atlas;[42,43,49] see Methods).
142 The detailed anatomical brain segmentation also allowed us to measure regional
143 XCI variability in each individual brain (Fig. 2; Supplementary Table 1), with the aim to
144 determine whether such variability is related to (or independent of) the overall whole-brain
145 Xm:Xp ratio, such as whether brains with highly skewed Xm:Xp ratios comprise different
146 (or the same) regional variability compared to brains with the overall Xm:Xp ratio close
147 equal. To investigate this question, we visualized regional variability in Xm and Xp
148 selection across all anatomical regions and for each brain in brain-wide 2D heatmaps (Fig.
149 2a) and collapsed box-and-whisker plots (Fig. 2b). This revealed a similar variability from
150 the mean for all imaged brains independent of their overall Xm:Xp ratio with the mean
151 coefficient of variations (CV) for both Mecp2-GFP(m/+) and Mecp2-GFP(p/+) groups
152 being ~20% compared to CV of ~10% in homozygous Mecp2-GFP(m/p) mice (Fig. 2c).
153 Taken together with the previous analyses, these data show that Xm versus Xp selection in
154 each brain can be described as a result of a modest overall bias favoring the selection of
155 the maternal X (and silencing of the paternal X) across all brain regions, combined with a
156 moderate ~20% local stochastic variability independent of the overall selection.
157
158
159 **Paternal XCI bias gates FXS disease penetrance**

160 Having quantified the XCI patterns in WT mice, we next asked whether the identified
161 biases may affect disease penetrance in a female heterozygous mouse model of the fragile
162 X syndrome (FXS), an X-linked disorder caused by the loss of expression of the Fragile
163 X mental retardation 1 (Fmr1) protein[18,50]. Based on the WT data, we envisioned the
164 following scenarios: First, the average ~60:40 bias favoring maternal X selection should
165 lead to more brain cells carrying the mutant allele inherited from the mother than from
166 the father, resulting in more pronounced phenotypes associated with the maternal
167 transmission. Second, stochastic variability in regional Xm:Xp selection may further
168 modify the phenotypic outcomes based on which brain areas comprise the least favorable
169 mutant-to-healthy X ratios. On the other hand, a positive selection for cells with the
170 healthy X chromosome may change the XCI distribution from what is seen in WT brain,
171 resulting in lesser than expected skewing and related phenotypes.

172 To test these scenarios, we crossed the Fmr1 knock-out (KO) mouse model of
173 FXS[51] with the Mecp2-GFP X reporter line, generating heterozygous Fmr1-KO/+ female
174 mice with the KO allele inherited either maternally in Fmr1-KO(m)/Mecp2-GFP(p) mice
175 or paternally in Fmr1-KO(p)/Mecp2-GFP(m) mice (Fig. 3a). We note that while this FXS
176 mouse model has been studied extensively as a complete knock-out in male hemizygous
177 Fmr-1 KO/Y mice, only three studies reported modest phenotypes (synaptic and social) in
178 female heterozygous Fmr1 KO/+ mice with the KO allele always transmitted maternally[52-
179 54]. Hence, our study is the first to directly compare the phenotypic effect of maternal versus
180 paternal Fmr1 KO allele transmission in heterozygous female mice, while also quantifying
181 the whole-brain distribution of the Fmr1-KO allele-expressing cells in each animal.

182 We first assayed the impact of the maternal versus paternal Fmr1-KO allele
183 transmission across three behavioral tests that were used previously to identify disease-
184 related phenotypes in FXS mice: the open field (OFT) test to assess sensorimotor functions
185 and anxiety-related behavior[55-61]; the T-maze spontaneous alternation test to assess working
186 memory[60,62,63]; and finally the 3-chamber test to assay sociability and social preference[61,64,65]
187 (Fig. 3b). Strikingly, these experiments revealed that while the Fmr1-KO(m)/Mecp2-
188 GFP(p) heterozygous female mice with maternal KO allele transmission showed deficits
189 in all three tests, whereas the paternal Fmr1-KO(p)/Mecp2-GFP(m) heterozygous mice
190 were not different from control Mecp2-GFP sibling mice in any measurement (Fig. 3c-g).

191 The behavioral deficits of the maternal Fmr1-KO(m)/Mecp2-GFP(p) mice included: 1)
192 reduced travel distance across the center arena in the OFT suggesting reduced exploratory
193 behavior due to sensorimotor deficits and/or increased anxiety (Fig. 3c), 2) reduced
194 frequency of spontaneous alterations in the T-maze suggesting impaired working memory
195 (Fig. 3d), and 3) a complete lack of social preference in the 3-chamber social interaction
196 test, reflected by no preference for time spent in the chamber with a stranger mouse
197 presented under a wire cup versus the control chamber comprising only an empty cup (Fig.
198 3e-g). Interestingly, the maternal Fmr1-KO(m)/Mecp2-GFP(p) mice were also hyperactive
199 in the 3-chamber apparatus, as reflected by an increased total distance traveled compared
200 to control Mecp2-GFP sibling mice, and this hyperactivity was restricted to the starting
201 middle chamber (Fig. 3f, g). This suggests a more complex social phenotype of a combined
202 hyperactivity and avoidance of both social and non-social stimuli in Fmr1-KO(m)/Mecp2-
203 GFP(p) mice.
204 Taken together, our behavioral results demonstrate that female mice with the Fmr1
205 KO allele transmitted maternally, but not paternally, display disease-related phenotypes.
206 This, in turn, suggests that the bias of higher maternal X selection (and higher paternal X
207 silencing) seen in WT mice persists in the heterozygous Fmr1-KO/+ mice and results in
208 more brain cells carrying the Fmr1 KO allele inherited maternally than paternally. To test
209 this prediction directly, we imaged the brains of all mice used in the above behavioral tests
210 by STPT as done for WT brains in Fig. 1 and determined the distribution of the WT Fmr1
211 allele-expressing cells marked by Mecp2-GFP expression from the same X chromosome.
212 These measurements revealed the following. First, the whole-brain Xm:Xp ratio in the
213 maternal Fmr1-KO(m)/Mecp2-GFP(p) mice was 54:46, representing an average 54% of
214 Fmr1-KO allele expressing brain cells compared to 46% Fmr1 WT allele expressing cells
215 (Fig. 3h, i; Supplementary Table 3, 4). Second, the regional Xm:Xp ratio differences were
216 more pronounced for cortical versus subcortical areas (Extended Data Fig. 3), suggesting
217 a modest compensation favoring the selection of the healthy paternal Xp chromosome
218 subcortically compared to WT brains. And third, the whole-brain Xm:Xp ratio in the
219 paternal Fmr1-KO(p)/Mecp2-GFP(m) mice was 41:59, reflecting an average 41% of Fmr1-
220 KO allele expressing brain cells compared to 59% Fmr1 WT allele expressing cells (Fig.
221 3h-i). These data thus demonstrate that an average ~55:45 mutant to healthy brain cell

222 density ratio is sufficient to cause behavioral phenotypes in the maternal Fmr1-
223 KO(m)/Mecp2-GFP(p) mice, while in contrast ~40:60 mutant to healthy brain cell density
224 ratio is below a threshold needed to produce phenotypic manifestations in the paternal
225 Fmr1-KO(p)/Mecp2-GFP(m) mice.
226

227 **Local XCI variability contributes to phenotypic diversity**

228 Brain-wide cellular distribution measurements of Fmr1 WT versus KO alleles allowed us
229 to further test whether regional stochastic XCI variability may further influence the
230 observed phenotypes in the affected maternal Fmr1-KO(m)/Mecp2-GFP(p) mice. For
231 example, it may be expected that mice with high Fmr1-KO allele cell density in brain areas
232 known to regulate social behavior will show more pronounced phenotypes in the 3-
233 chamber sociability test compared to those with a stochastically lower Fmr1 KO allele cell
234 density in the same brain areas. To test this hypothesis, we correlated the Fmr1 WT:KO
235 cell ratios across all brain regions to behavioral scores from all three behaviors for each
236 mouse tested. This correlation analysis identified two distinct sets of anatomical regions in
237 the maternal Fmr1-KO(m)/Mecp2-GFP(p) brains, in which the Fmr1 WT:KO cell ratios
238 were indeed correlated to behavioral performance in either the OFT or the 3-chamber test
239 (Fig. 4a; Extended Data Fig. 4).

240 The first set of brain regions comprised areas in which the Fmr1 WT:KO cell ratio
241 was positively correlated to OFT behavioral performance, specifically the distance traveled
242 in the center of the OFT arena. These regions included primarily sensory structures of the
243 thalamus, midbrain and hindbrain (Fig. 4a, d-f; Extended Data Fig 4a; Supplementary
244 Table 5), such as the sensory ventral posterolateral nucleus of the thalamus (VPL) (Fig 4b).
245 These data thus indicate that a higher density of cells expressing the Fmr1 WT allele across
246 the identified areas known to regulate sensorimotor functions, among others, translates to
247 increased exploration of the open field arena and hence a reduced OFT phenotype. The
248 second set of brain regions comprised areas in which the Fmr1 WT:KO cell ratio was
249 inversely correlated to the time spent in the center of the 3-chamber apparatus. These
250 regions, in contrast to the first set, contained primarily cortical, hippocampal and
251 hypothalamic brain areas (Fig. 4a, c, g-i; Extended Data Fig. 4a; Supplementary Table 5),
252 including the hypothalamic medial preoptic nucleus (MPN) that is well known for

253 regulating social behavior (Fig 4c; Extended Data Fig 4c). These data, in turn, indicate that
254 a higher density of cells expressing the Fmr1 KO allele across areas known to regulate
255 social behaviors, among others, translates to more time spent in the starting chamber of the
256 3-chamber apparatus and hence a more pronounced social deficit phenotype. The same
257 correlation analysis failed to identify a distinct set of brain regions with Fmr1 WT:KO
258 ratios related to behavioral performance in the T-maze test in which the Fmr1-
259 KO(m)/Mecp2-GFP(p) mice showed only a modest level of impairment (Fig. 3a;
260 Supplementary Table 5). In addition, whole-brain Fmr1 WT:KO ratios, in contrast to the
261 regional ratios described above, showed only a trend towards a positive correlation in the
262 OFT and negative correlation in the 3-chamber task (Extended Data Fig. 5). This suggests
263 that while the whole-brain WT:KO cell ratios set the overall risk for disease penetrance,
264 the regional Fmr1 WT:KO cell ratios determine the specific behavioral phenotypic
265 outcome in each animal. Finally, as expected, we also did not observe any significant
266 correlations for brain regions in the paternal Fmr1-KO(p)/Mecp2-GFP(m) mice which did
267 not show any behavioral phenotypes (Fig. 4a; Supplementary Table 5).
268

269 **Anatomical brain networks underlying distinct behavioral phenotypes**

270 The identification of the two sets of brain regions with Fmr1 KO allele density linked to
271 behavioral phenotypes suggests that these represent two distinct anatomically connected
272 brain networks regulating sensorimotor and anxiety-related versus social behaviors. To test
273 this hypothesis further, we next applied the recently established structural connectivity
274 matrix analysis derived from a whole-brain connectivity model of the mouse brain[66] (See
275 methods). This analysis indeed revealed much higher connection densities for brain regions
276 within each brain network than for matching randomly sampled brain structures: the OFT
277 network density (Fig. 5a-b) and 3-chamber network density (Fig. 5e-f) represented the 93rd
278 and 100th percentile of each sample network's distribution, respectively (Supplementary
279 Table 6; see Methods). This analysis thus supports the model where the brain areas with
280 Fmr1-KO cell density linked to different behavioral deficits represent two distinct
281 functional brain networks.

282 The identified correlations of local Fmr1-KO cell densities to behavioral
283 phenotypes also suggest that the distribution of the Fmr1-KO allele across the two brain

284 networks determines and can in fact predict the disease penetrance in each animal. To test
285 this hypothesis, we next calculated the Fmr1 WT:KO allele ratios selectively across the
286 two brain networks and regressed these values against the behavioral performance in the
287 OFT and 3-chamber test (Supplementary Table 7). As shown in Fig. 5, the Fmr1 WT:KO
288 allele ratios were indeed highly significant predictors of individual behavioral performance
289 in only maternal Fmr1-KO(m)/Mecp2-GFP(p) heterozygous mice in both the OFT (Fig.
290 5c) and 3-chamber (Fig. 5g) assays, and not for control or paternal Frm1-KO(p)/Mecp2-
291 GFP(m) mice (Extended Data Fig. 6. These data thus further support the model where the
292 cellular distribution of the Fmr1-KO allele across the two brain networks represent the
293 cellular and genetic substrate the respective OFT and 3-chamber test behavioral
294 phenotypes.

295 Finally, in the last set of analyses, we asked what is the local Fmr1 KO cell density
296 that can differentiate normal from disease-related behavior. Likelihood-ratio tests
297 performed on binary logistic regression models revealed that the Fmr1-KO allele
298 distributions across the brain networks indeed significantly predicts normal from disease-
299 related performance in both the OFT (Fig. 5d) and 3-chamber test (Fig. 5h). The equal-
300 odds ratio of normal versus disease-related behavioral outcome was calculated to be 55.20
301 ± 5.95% healthy cell density percent in the OFT brain network and 49.18 ± 5.19% healthy
302 cell density percent in the 3-chamber brain network. This phenotypic penetrance threshold
303 of ~50% regional Fmr1-KO cell density agrees with the lack of behavioral manifestations
304 when the Fmr1-KO allele is transmitted paternally in ~40% brain cells (Fig 3).
305

306 **Discussion**

307 We applied our automated whole-brain imaging platform[42] to comprehensively quantify
308 the respective distributions of active maternal and paternal X chromosomes across the
309 entire mouse brain at single cell resolution. This approach allowed us to discover subtle
310 yet both statistically and functionally significant patterns that were missed by previous
311 studies relying on semiquantitative observations typically from only a few selected brain
312 areas[48,67-69].

313 Clinical studies of the effects of XCI skewing on neurodevelopmental disorders
314 typically consider >80% (or even >90%) skewing in favor of the healthy X chromosome

315 as significant with respect to modifying X-linked phenotypes, with ratios below the 80%
316 threshold defined as balanced (i.e., non-skewed)[1-10]. Therefore, these studies suggest that
317 brain development can tolerate only 10 to 20% of brain cells carrying a deleterious
318 mutation and a higher percentage of affected brain cells should be expected to lead to
319 clinical manifestations. In contrast, our study revealed a lack of behavioral phenotypes in
320 paternal heterozygous Fmr1-KO(p)/+ mice carrying the Fmr1-KO allele in ~40% brain
321 cells, demonstrating an unexpectedly robust brain capacity to compensate for the presence
322 of a harmful mutation in nearly half of brain cells. Therefore, we propose that a threshold
323 of ~60% skewing in favor of the healthy X chromosome may be sufficient for modifying
324 neurodevelopmental phenotypic penetrance and should be considered clinically relevant.
325 This suggests that negative results from many clinical studies that considered >80% XCI
326 skewing as a threshold for interpretating clinical phenotypes may need to be reevaluated
327 with the lower threshold >60% as a skewed XCI definition[5,37-40,70-76].

328 In addition to challenging the dogma that only large degree of XCI skewing can
329 affect X-linked neurodevelopmental phenotypes, our results also show that stochastic XCI
330 variability, estimated from our measurements to be ~20% across all brain regions
331 independent of the overall brain XCI bias, can play an important role in determining the
332 specific phenotypic manifestations in each individual female. Our data revealed that in the
333 maternal heterozygous Fmr1-KO(m)/+ mice, the Fmr1-KO allele variations across two
334 distinct brain networks can predict the likelihood of disease-related phenotypes in two
335 behavioral tests – the open field and 3-chamber test measuring sensorimotor performance
336 and sociability, respectively – in each animal. Thus, while the overall ~60% brain cell
337 transmission of the maternal Fmr1-KO allele predisposes for disease related phenotypes,
338 the ~20% stochastic brain-wide variation on top of the overall pattern is likely to determine
339 the specific features of the phenotypic representation (Fig 6). This finding provides an
340 important etiological insight into the potential source of phenotypic variability in X-linked
341 neurodevelopmental syndromes disease in female patients.

342 The finding that the brain can tolerate the loss of as important a gene as Fmr1 in
343 nearly half brain cells may also be relevant for the interpretation of the significance of
344 somatic mutations in the brain, which occur during cell divisions after fertilization and lead
345 to a mosaic expression of a genetic lesion in a subset of brain cells and cell types depending

346 on the cell lineages affected[77-80]. While some genetic lesions can lead to
347 neurodevelopmental phenotypes even when expressed in a relatively local cell population
348 in the brain, such mutations linked to focal epilepsy or gross morphological development[81-
349 87], our data suggest that mutations related to more cognitive dysfunctions in
350 neurodevelopment, such as those linked to autism or intellectual disability, may require a
351 similarly high threshold of >50% brain cells (perhaps within a specific cell type lineage)
352 to be affected to lead to phenotypic manifestations.

353 Finally, our results also suggest a novel evolutionary role of the observed 60:40
354 XCI paternal bias. Maternally and paternally imprinted autosomal genes are expressed in
355 highly distinct regional patterns proposed to mediate competing interests of each parent in
356 terms of the evolutionary fitness of their genes, as proposed in the so-called kinship or
357 genetic conflict theory[88,89]. Our study revealed a systematic ~60:40 paternal bias in XCI
358 across all brain divisions and regions, suggesting that XCI is not part of such a maternal
359 versus paternal genetic competition. On the other hand, the paternal XCI bias may play a
360 different evolutionary role. It is well established that the mutation rate in the paternal
361 germline is significantly higher compared to that in the maternal germ cells, which should
362 result in a higher rate of X-linked mutations linked to neurodevelopmental deficits from
363 paternal transmission[11-16]. Our findings thus suggest that the selective bias to silence ~60%
364 of the paternal X chromosome and the surprising developmental capacity to tolerate the
365 mutant allele in nearly half brain cells may in fact represent a novel evolutionary
366 mechanism acting to counter the higher frequency of *de novo* mutations inherited from the
367 father compared to the mother in daughters.

368 In the current study we used the Fmr1-KO allele as an established mouse model of
369 X-linked genetic lesion, but we note that human FXS is caused by expansion (>200 repeats)
370 of the 5' UTR CGG sequence of an FMR1 premutation allele inherited exclusively
371 maternally[18,90-92]. Therefore, the observed ~60:40 paternal XCI bias is not directly pertinent
372 to FXS inheritance, but instead may be evolutionary important in protecting offspring from
373 a higher rate of paternally inherited *de novo* mutations in one of the more than 130 X genes
374 linked to non-syndromic intellectual disability and other neurodevelopmental phenotypes[17-
375 23].
376

377
378

379 **Main References**

380

381 1 Ørstavik, K. H. X chromosome inactivation in clinical practice. *Human*
382 *genetics* **126**, 363–373 (2009).
383 2 Plenge, R. M., Stevenson, R. A., Lubs, H. A., Schwartz, C. E. & Willard, H. F.
384 Skewed X-chromosome inactivation is a common feature of X-linked mental
385 retardation disorders. *The American Journal of Human Genetics* **71**, 168–173
386 (2002).
387 3 Minks, J., Robinson, W. P. & Brown, C. J. A skewed view of X chromosome
388 inactivation. *The Journal of clinical investigation* **118**, 20–23 (2008).
389 4 Vianna, E. Q. *et al.* Understanding the landscape of X-linked variants causing
390 intellectual disability in females through extreme X chromosome inactivation
391 skewing. *Molecular neurobiology* **57**, 3671–3684 (2020).
392 5 Xiol, C. *et al.* X chromosome inactivation does not necessarily determine the
393 severity of the phenotype in Rett syndrome patients. *Scientific reports* **9**, 1–9
394 (2019).
395 6 Gibson, J. H., Williamson, S. L., Arbuckle, S. & Christodoulou, J. X
396 chromosome inactivation patterns in brain in Rett syndrome: implications
397 for the disease phenotype. *Brain and Development* **27**, 266–270 (2005).
398 7 Brown, C. J. Skewed X-chromosome inactivation: cause or consequence?
399 *Journal of the National Cancer Institute* **91**, 304–305 (1999).
400 8 Bittel, D. C. *et al.* Comparison of X-chromosome inactivation patterns in
401 multiple tissues from human females. *J Med Genet* **45**, 309–313,
402 doi:10.1136/jmg.2007.055244 (2008).
403 9 Shahbazian, M. D., Sun, Y. & Zoghbi, H. Y. Balanced X chromosome
404 inactivation patterns in the Rett syndrome brain. *American journal of medical*
405 *genetics* **111**, 164–168 (2002).
406 10 Renault, N. K. *et al.* Human X-chromosome inactivation pattern distributions
407 fit a model of genetically influenced choice better than models of completely
408 random choice. *European Journal of Human Genetics* **21**, 1396–1402 (2013).
409 11 Rahbari, R. *et al.* Timing, rates and spectra of human germline mutation.
410 *Nature genetics* **48**, 126–133 (2016).
411 12 Jónsson, H. *et al.* Parental influence on human germline de novo mutations in
412 1,548 trios from Iceland. *Nature* **549**, 519–522 (2017).

13 Crow, J. F. The origins, patterns and implications of human spontaneous mutation. *Nature Reviews Genetics* **1**, 40–47 (2000).

14 Conrad, D. F. *et al.* Variation in genome–wide mutation rates within and between human families. *Nature genetics* **43**, 712 (2011).

15 Kong, A. *et al.* Rate of de novo mutations and the importance of father's age to disease risk. *Nature* **488**, 471–475 (2012).

16 Gao, Z. *et al.* Overlooked roles of DNA damage and maternal age in generating human germline mutations. *Proceedings of the National Academy of Sciences* **116**, 9491–9500 (2019).

17 Nguyen, D. K. & Disteche, C. M. Dosage compensation of the active X chromosome in mammals. *Nat Genet* **38**, 47–53, doi:10.1038/ng1705 (2006).

18 Verkerk, A. J. *et al.* Identification of a gene (FMR–1) containing a CGG repeat coincident with a breakpoint cluster region exhibiting length variation in fragile X syndrome. *Cell* **65**, 905–914 (1991).

19 Ropers, H. H. & Hamel, B. C. X–linked mental retardation. *Nat Rev Genet* **6**, 46–57, doi:10.1038/nrg1501 (2005).

20 Skuse, D. H. X–linked genes and mental functioning. *Hum Mol Genet* **14 Spec No 1**, R27–32, doi:10.1093/hmg/ddi112 (2005).

21 Neri, G., Schwartz, C. E., Lubs, H. A. & Stevenson, R. E. X - linked intellectual disability update 2017. *American Journal of Medical Genetics Part A* **176**, 1375–1388 (2018).

22 Chiurazzi, P., Schwartz, C. E., Gecz, J. & Neri, G. XLMR genes: update 2007. *European Journal of Human Genetics* **16**, 422–434 (2008).

23 Thormann, A. *et al.* Flexible and scalable diagnostic filtering of genomic variants using G2P with Ensembl VEP. *Nature communications* **10**, 1–10 (2019).

24 Lyon, M. F. Gene action in the X–chromosome of the mouse (Mus musculus L.). *Nature* **190**, 372–373 (1961).

25 Lyon, M. F. X–chromosome inactivation and developmental patterns in mammals. *Biol Rev Camb Philos Soc* **47**, 1–35 (1972).

26 Avner, P. & Heard, E. X–chromosome inactivation: counting, choice and initiation. *Nat Rev Genet* **2**, 59–67, doi:10.1038/35047580 (2001).

27 Gartler, S. M. & Riggs, A. D. Mammalian X–chromosome inactivation. *Annu Rev Genet* **17**, 155–190, doi:10.1146/annurev.ge.17.120183.001103 (1983).

28 Archer, H. *et al.* Correlation between clinical severity in patients with Rett syndrome with a p. R168X or p. T158M MECP2 mutation, and the direction and degree of skewing of X–chromosome inactivation. *Journal of medical genetics* **44**, 148–152 (2007).

29 Wan, M. *et al.* Rett syndrome and beyond: recurrent spontaneous and familial MECP2 mutations at CpG hotspots. *The American Journal of Human Genetics* **65**, 1520–1529 (1999).

30 Amir, R. E. *et al.* Influence of mutation type and X chromosome inactivation on Rett syndrome phenotypes. *Annals of neurology* **47**, 670–679 (2000).

31 Villard, L. *et al.* Two affected boys in a Rett syndrome family: clinical and molecular findings. *Neurology* **55**, 1188–1193 (2000).

32 Zappella, M., Meloni, I., Longo, I., Hayek, G. & Renieri, A. Preserved speech variants of the Rett syndrome: molecular and clinical analysis. *American journal of medical genetics* **104**, 14–22 (2001).

33 Bienvenu, T. *et al.* MECP2 mutations account for most cases of typical forms of Rett syndrome. *Human Molecular Genetics* **9**, 1377–1384 (2000).

34 Heine - Suñer, D. *et al.* Fragile - X syndrome and skewed X - chromosome inactivation within a family: A female member with complete inactivation of the functional X chromosome. *American Journal of Medical Genetics Part A* **122**, 108–114 (2003).

35 Van Esch, H. *et al.* Duplication of the MECP2 region is a frequent cause of severe mental retardation and progressive neurological symptoms in males. *The American Journal of Human Genetics* **77**, 442–453 (2005).

36 Zoghbi, H. Y., Percy, A. K., Schultz, R. J. & Fill, C. Patterns of X chromosome inactivation in the Rett syndrome. *Brain and Development* **12**, 131–135 (1990).

37 Smeets, E. *et al.* Rett syndrome in adolescent and adult females: clinical and molecular genetic findings. *American Journal of Medical Genetics Part A* **122**, 227–233 (2003).

38 Sirianni, N., Naidu, S., Pereira, J., Pillotto, R. F. & Hoffman, E. P. Rett syndrome: confirmation of X–linked dominant inheritance, and localization of the gene to Xq28. *American journal of human genetics* **63**, 1552 (1998).

39 Auranen, M. *et al.* MECP2 gene analysis in classical Rett syndrome and in patients with Rett–like features. *Neurology* **56**, 611–617 (2001).

40 Nielsen, J. B. *et al.* MECP2 mutations in Danish patients with Rett syndrome: high frequency of mutations but no consistent correlations with clinical

severity or with the X chromosome inactivation pattern. *European Journal of Human Genetics* **9**, 178 (2001).

41 Taylor, A. K. *et al.* Molecular predictors of cognitive involvement in female carriers of fragile X syndrome. *Jama* **271**, 507–514 (1994).

42 Kim, Y. *et al.* Brain-wide Maps Reveal Stereotyped Cell-Type-Based Cortical Architecture and Subcortical Sexual Dimorphism. *Cell* **171**, 456–469 e422, doi:10.1016/j.cell.2017.09.020 (2017).

43 Kim, Y. *et al.* Mapping social behavior-induced brain activation at cellular resolution in the mouse. *Cell Rep* **10**, 292–305, doi:10.1016/j.celrep.2014.12.014 (2015).

44 Ragan, T. *et al.* Serial two-photon tomography for automated ex vivo mouse brain imaging. *Nat Methods* **9**, 255–258 (2012).

45 Brown, K. *et al.* The molecular basis of variable phenotypic severity among common missense mutations causing Rett syndrome. *Human molecular genetics* **25**, 558–570 (2015).

46 Lyst, M. J. *et al.* Rett syndrome mutations abolish the interaction of MeCP2 with the NCoR/SMRT co-repressor. *Nature neuroscience* **16**, 898 (2013).

47 Linhoff, M. W., Garg, S. K. & Mandel, G. A high-resolution imaging approach to investigate chromatin architecture in complex tissues. *cell* **163**, 246–255 (2015).

48 Gregg, C., Zhang, J., Butler, J. E., Haig, D. & Dulac, C. Sex-specific parent-of-origin allelic expression in the mouse brain. *Science* **329**, 682–685 (2010).

49 Dong, H. W. *The Allen reference atlas: A digital color brain atlas of the C57Bl/6J male mouse*. (John Wiley & Sons Inc, 2008).

50 Pieretti, M. *et al.* Absence of expression of the FMR-1 gene in fragile X syndrome. *Cell* **66**, 817–822 (1991).

51 Bakker, C. E. *et al.* Fmr1 knockout mice: a model to study fragile X mental retardation. *Cell* **78**, 23–33 (1994).

52 Gauducheau, M. *et al.* Age-specific autistic-like behaviors in heterozygous Fmr1-KO female mice. *Autism Res* **10**, 1067–1078, doi:10.1002/aur.1743 (2017).

53 Yau, S. Y. *et al.* Impaired bidirectional NMDA receptor dependent synaptic plasticity in the dentate gyrus of adult female Fmr1 heterozygous knockout mice. *Neurobiol Dis* **96**, 261–270, doi:10.1016/j.nbd.2016.09.012 (2016).

54 Nolan, S. O., Hodges, S. L. & Lugo, J. N. High‐throughput analysis of vocalizations reveals sex‐specific changes in Fmr1 mutant pups. *Genes, Brain and Behavior* (2019).

55 Peier, A. M. *et al.* (Over)correction of FMR1 deficiency with YAC transgenics: behavioral and physical features. *Hum Mol Genet* **9**, 1145–1159, doi:10.1093/hmg/9.8.1145 (2000).

56 Chen, L. & Toth, M. Fragile X mice develop sensory hyperreactivity to auditory stimuli. *Neuroscience* **103**, 1043–1050, doi:10.1016/s0306-4522(01)00036-7 (2001).

57 Yan, Q. J., Asafo-Adjei, P. K., Arnold, H. M., Brown, R. E. & Bauchwitz, R. P. A phenotypic and molecular characterization of the fmr1-tm1Cgr fragile X mouse. *Genes Brain Behav* **3**, 337–359, doi:10.1111/j.1601-183X.2004.00087.x (2004).

58 Restivo, L. *et al.* Enriched environment promotes behavioral and morphological recovery in a mouse model for the fragile X syndrome. *Proc Natl Acad Sci U S A* **102**, 11557–11562, doi:10.1073/pnas.0504984102 (2005).

59 Olmos-Serrano, J. L. & Corbin, J. G. Amygdala regulation of fear and emotionality in fragile X syndrome. *Dev Neurosci* **33**, 365–378, doi:10.1159/000329424 (2011).

60 Santos, A. R., Kanellopoulos, A. K. & Bagni, C. Learning and behavioral deficits associated with the absence of the fragile X mental retardation protein: what a fly and mouse model can teach us. *Learn Mem* **21**, 543–555, doi:10.1101/lm.035956.114 (2014).

61 Nolan, S. O. *et al.* Deletion of Fmr1 results in sex-specific changes in behavior. *Brain Behav* **7**, e00800, doi:10.1002/brb3.800 (2017).

62 Oddi, D. *et al.* Early social enrichment rescues adult behavioral and brain abnormalities in a mouse model of fragile X syndrome. *Neuropsychopharmacology* **40**, 1113–1122, doi:10.1038/npp.2014.291 (2015).

63 Udagawa, T. *et al.* Genetic and acute CPEB1 depletion ameliorate fragile X pathophysiology. *Nat Med* **19**, 1473–1477, doi:10.1038/nm.3353 (2013).

64 Naviaux, J. C. *et al.* Reversal of autism-like behaviors and metabolism in adult mice with single-dose antipurinergic therapy. *Transl Psychiatry* **4**, e400, doi:10.1038/tp.2014.33 (2014).

554 65 Liu, Z. H. & Smith, C. B. Dissociation of social and nonsocial anxiety in a
555 mouse model of fragile X syndrome. *Neurosci Lett* **454**, 62–66,
556 doi:10.1016/j.neulet.2009.02.066 (2009).
557 66 Knox, J. E. *et al.* High–resolution data–driven model of the mouse
558 connectome. *Network Neuroscience* **3**, 217–236 (2018).
559 67 Watson, C. M. *et al.* Reduced proportion of Purkinje cells expressing
560 paternally derived mutant Mecp2 308 allele in female mouse cerebellum is
561 not due to a skewed primary pattern of X–chromosome inactivation. *Human*
562 *molecular genetics* **14**, 1851–1861 (2005).
563 68 Wu, H. *et al.* Cellular resolution maps of X chromosome inactivation:
564 implications for neural development, function, and disease. *Neuron* **81**, 103–
565 119, doi:10.1016/j.neuron.2013.10.051 (2014).
566 69 Sugimoto, M., Tan, S.–S. & Takagi, N. X chromosome inactivation revealed by
567 the X–linked lacZ transgene activity in periimplantation mouse embryos.
568 *International Journal of Developmental Biology* **44**, 177–182 (2002).
569 70 Kerr, A., Archer, H., Evans, J., Prescott, R. & Gibbon, F. People with MECP2
570 mutation‐positive Rett disorder who converse. *Journal of Intellectual*
571 *Disability Research* **50**, 386–394 (2006).
572 71 Bijlsma, E. *et al.* Xq28 duplications including MECP2 in five females:
573 Expanding the phenotype to severe mental retardation. *European journal of*
574 *medical genetics* **55**, 404–413 (2012).
575 72 Vacca, M., Della Ragione, F., Scalabrì, F. & DEsposito, M. in *Seminars in cell &*
576 *developmental biology*. 78–87 (Elsevier).
577 73 Grasshoff, U. *et al.* De novo MECP2 duplication in two females with random
578 X–inactivation and moderate mental retardation. *European Journal of Human*
579 *Genetics* **19**, 507–512 (2011).
580 74 Amos–Landgraf, J. M. *et al.* X chromosome–inactivation patterns of 1,005
581 phenotypically unaffected females. *The American Journal of Human Genetics*
582 **79**, 493–499 (2006).
583 75 Tukiainen, T. *et al.* Landscape of X chromosome inactivation across human
584 tissues. *Nature* **550**, 244–248 (2017).
585 76 Fieremans, N. *et al.* Identification of intellectual disability genes in female
586 patients with a skewed X‐inactivation pattern. *Human mutation* **37**, 804–
587 811 (2016).
588 77 Poduri, A., Evrony, G. D., Cai, X. & Walsh, C. A. Somatic mutation, genomic
589 variation, and neurological disease. *Science* **341** (2013).

590 78 McConnell, M. J. *et al.* Intersection of diverse neuronal genomes and
591 neuropsychiatric disease: The Brain Somatic Mosaicism Network. *Science*
592 **356** (2017).
593 79 Paquola, A. C., Erwin, J. A. & Gage, F. H. Insights into the role of somatic
594 mosaicism in the brain. *Current opinion in systems biology* **1**, 90–94 (2017).
595 80 Bedrosian, T. A., Linker, S. & Gage, F. H. Environment-driven somatic
596 mosaicism in brain disorders. *Genome medicine* **8**, 1–4 (2016).
597 81 Gennaro, E. *et al.* Somatic and germline mosaicisms in severe myoclonic
598 epilepsy of infancy. *Biochemical and biophysical research communications*
599 **341**, 489–493 (2006).
600 82 Vadlamudi, L. *et al.* Timing of de novo mutagenesis—a twin study of sodium-
601 channel mutations. *New England Journal of Medicine* **363**, 1335–1340
602 (2010).
603 83 Gleeson, J. G. *et al.* Somatic and germline mosaic mutations in the
604 doublecortin gene are associated with variable phenotypes. *The American*
605 *Journal of Human Genetics* **67**, 574–581 (2000).
606 84 Hua, Y. & Crino, P. B. Single cell lineage analysis in human focal cortical
607 dysplasia. *Cerebral Cortex* **13**, 693–699 (2003).
608 85 Rivière, J.-B. *et al.* De novo germline and postzygotic mutations in AKT3,
609 PIK3R2 and PIK3CA cause a spectrum of related megalencephaly syndromes.
610 *Nature genetics* **44**, 934–940 (2012).
611 86 Poduri, A. *et al.* Somatic activation of AKT3 causes hemispheric
612 developmental brain malformations. *Neuron* **74**, 41–48 (2012).
613 87 Lee, J. H. *et al.* De novo somatic mutations in components of the PI3K-AKT3-
614 mTOR pathway cause hemimegalencephaly. *Nature genetics* **44**, 941–945
615 (2012).
616 88 Moore, T. & Haig, D. Genomic imprinting in mammalian development: a
617 parental tug-of-war. *Trends in genetics : TIG* **7**, 45–49, doi:10.1016/0168-
618 9525(91)90230-N (1991).
619 89 Haig, D. The kinship theory of genomic imprinting. *Annual review of ecology*
620 *and systematics* **31**, 9–32 (2000).
621 90 Penagarikano, O., Mulle, J. G. & Warren, S. T. The pathophysiology of fragile x
622 syndrome. *Annu. Rev. Genomics Hum. Genet.* **8**, 109–129 (2007).
623 91 Pembrey, M., Winter, R., Davies, K., Opitz, J. M. & Reynolds, J. F. A
624 premutation that generates a defect at crossing over explains the inheritance

of fragile X mental retardation. *American journal of medical genetics* **21**, 709–717 (1985).

92 Malter, H. E. *et al.* Characterization of the full fragile X syndrome mutation in fetal gametes. *Nature genetics* **15**, 165–169 (1997).

93 Brown, K. *et al.* The molecular basis of variable phenotypic severity among common missense mutations causing Rett syndrome. *Hum Mol Genet* **25**, 558–570, doi:10.1093/hmg/ddv496 (2016).

94 McLeod, F. *et al.* Reduced seizure threshold and altered network oscillatory properties in a mouse model of Rett syndrome. *Neuroscience* **231**, 195–205, doi:10.1016/j.neuroscience.2012.11.058 (2013).

95 Turaga, S. C. *et al.* Convolutional networks can learn to generate affinity graphs for image segmentation. *Neural Comput* **22**, 511–538 (2010).

96 Mattes, D., Haynor, D. R., Vesselle, H., Lewellen, T. K. & Eubank, W. PET–CT image registration in the chest using free–form deformations. . *IEEE Transactions in Medical Imaging* **22**, 120 – 128 (2003).

97 Klein, S., Staring, M., Murphy, K., Viergever, M. A. & Pluim, J. P. elastix: a toolbox for intensity–based medical image registration. *IEEE Trans Med Imaging* **29**, 196–205, doi:10.1109/TMI.2009.2035616 (2010).

98 Williams, R. W. & Rakic, P. Three–dimensional counting: an accurate and direct method to estimate numbers of cells in sectioned material. *J Comp Neurol* **278**, 344–352, doi:10.1002/cne.902780305 (1988).

99 Deacon, R. M. & Rawlins, J. N. T–maze alternation in the rodent. *Nat Protoc* **1**, 7–12, doi:10.1038/nprot.2006.2 (2006).

100 Spowart–Manning, L. & van der Staay, F. J. The T–maze continuous alternation task for assessing the effects of putative cognition enhancers in the mouse. *Behav Brain Res* **151**, 37–46, doi:10.1016/j.bbr.2003.08.004 (2004).

101 Oh, S. W. *et al.* A mesoscale connectome of the mouse brain. *Nature* **508**, 207–214, doi:10.1038/nature13186 (2014).

102 Yang, M., Silverman, J.L., & Crawley, J.N. Automated three-chambered social approach task for mice. *Curr Protoc Neurosci* **Chapter 8**: Unit 8.26 (2011)

Supplemental Tables

Table 1: Brain-wide descriptive statistics of cell counts, volumes, and cell densities

Table 2: Brain-wide statistical results of Xm-active versus Xp-active cell density comparisons

Table 3. Brain-wide descriptive statistics of cell counts, volumes, and cell densities

Table 4. Statistical results of brain-wide cell density comparisons in Fmr1 WT or heterozygous KO mice

Table 5: Statistical results of brain-wide ROI cell density and behavioral score correlational screens

Table 6: Normalized ROI connection density matrices

Table 7: ROI networks of penetrance raw data

Figures and Figure Legends

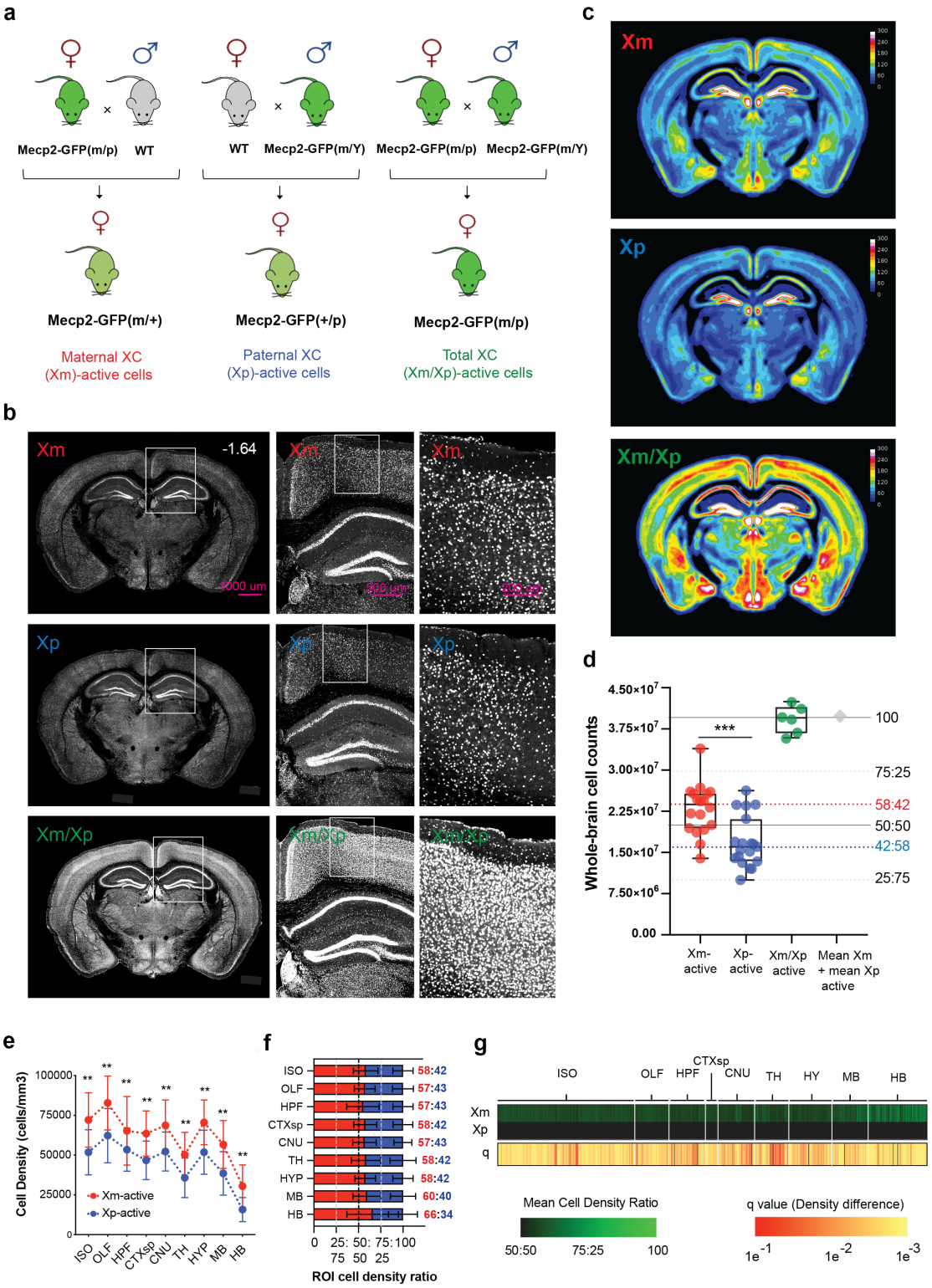

Fig. 1 | Whole-brain quantification of active maternal and paternal X chromosome distribution. a, Strategy for breeding maternal, paternal, and homozygous Mecp2-GFP

698 reporter mice. Left: heterozygous Mecp2-GFP(m/+) females with maternal Mecp2-GFP
699 allele are derived from breeding homozygous female Mecp2-GFP(m/p) and WT male
700 mice. Middle: heterozygous Mecp2-GFP(p/+) females with paternal Mecp2-GFP allele are
701 derived from breeding WT female and hemizygous Mecp2-GFP(m/Y) male mice. Right:
702 homozygous Mecp2-GFP(m/p) mice are derived from breeding Mecp2-GFP(m/p) female
703 and Mecp2-GFP(m/Y) male mice. **b**, Representative STPT images from brains with
704 maternal Xm-Mecp2-GFP (top), paternal Xp-Mecp2-GFP (middle) and homozygous Xm-
705 Mecp2-GFP/Xp-Mecp2-GFP (bottom) cells. **c**, Mecp2-GFP+ cell density in the three
706 genotypes represented as voxelized heat maps of a 16-color gradient scale from black (0
707 cells/voxel), yellow (150 cells/voxel) to white (300 cells/100 μm sphere voxel). **d**, Whole-
708 brain Mecp2-GFP+ cell counts (mean ± SD): Xm-GFP+ cells = $2.34 \times 10^7 \pm 4.96 \times 10^6$
709 (n=18); Xp-GFP+ cells = $1.69 \times 10^7 \pm 4.63 \times 10^6$ (n=19); and homozygous Xm-GFP+/Xp-
710 GFP+ cells = $3.92 \times 10^7 \pm 2.52 \times 10^6$ (n=6); $p = 0.00023$, Welch's t test. The sum of the
711 heterozygous Xm-GFP+ and Xp-GFP+ cell counts is shown as a black diamond. Solid
712 horizonal lines indicate 100% and 50% of homozygous Xm-GFP/Xp-GFP cell count.
713 Dashed gray lines indicate 75:25 and 25:75 Xm-active:Xp-active cell ratios based on the
714 homozygous Xm-GFP/Xp-GFP cell count. Dashed red and blue lines show the derived
715 mean 58:42 Xm-active:Xp-active and 42:58 Xp-active:Xm-active ratios. **e**, Xm-active
716 (red) and Xp-active (blue) cell densities (cells/mm^3) demonstrate a comparable Xm
717 selection bias across all major ontological brain divisions (mean ± SD; Xm-active, Xp-
718 active): ISO (isocortex): 72118 ± 17083, 51810 ± 14188; OLF (olfactory areas): 82791 ±
719 16950, 62260 ± 17057; HPF (hippocampal formation): 65273 ± 21583, 53398 ± 13519;
720 CTXsp (cortical subplate): 63541 ± 14215, 46708 ± 12138; CNU (cerebral nuclei): 68663
721 ± 16025, 52269 ± 12254; TH (thalamus): 50224 ± 14088, 35745 ± 12424; HY
722 (hypothalamus): 70594 ± 14086, 51834 ± 13835; MB: 56670 ± 15046, 38513 ±1364; HB
723 (hindbrain): 30458 ± 13392, 15766 ± 7539; $^{**}p < 0.01$, 2-way mixed effects ANOVA
724 with Holm-Sidak corrected post-hoc comparisons. **f**, Data from **e**, converted into cell
725 density ratios reveal ~60:40 Xm-active bias across all regions. Ratios for each ROI are
726 listed to the right and color-coded by Xm-active (red) and Xp-active (blue) samples. **g**, Xm
727 selection bias is seen across all brain regions. Left two columns: Heat map visualization of

normalized mean Xm-active and Xp-active ROI cell density on a color gradient of black (50%) to green (100%). Right column: statistical significance across all ROIs (FDR-corrected student's t tests), with each q value indicated by a color gradient from red (0.1) to yellow (0.001).

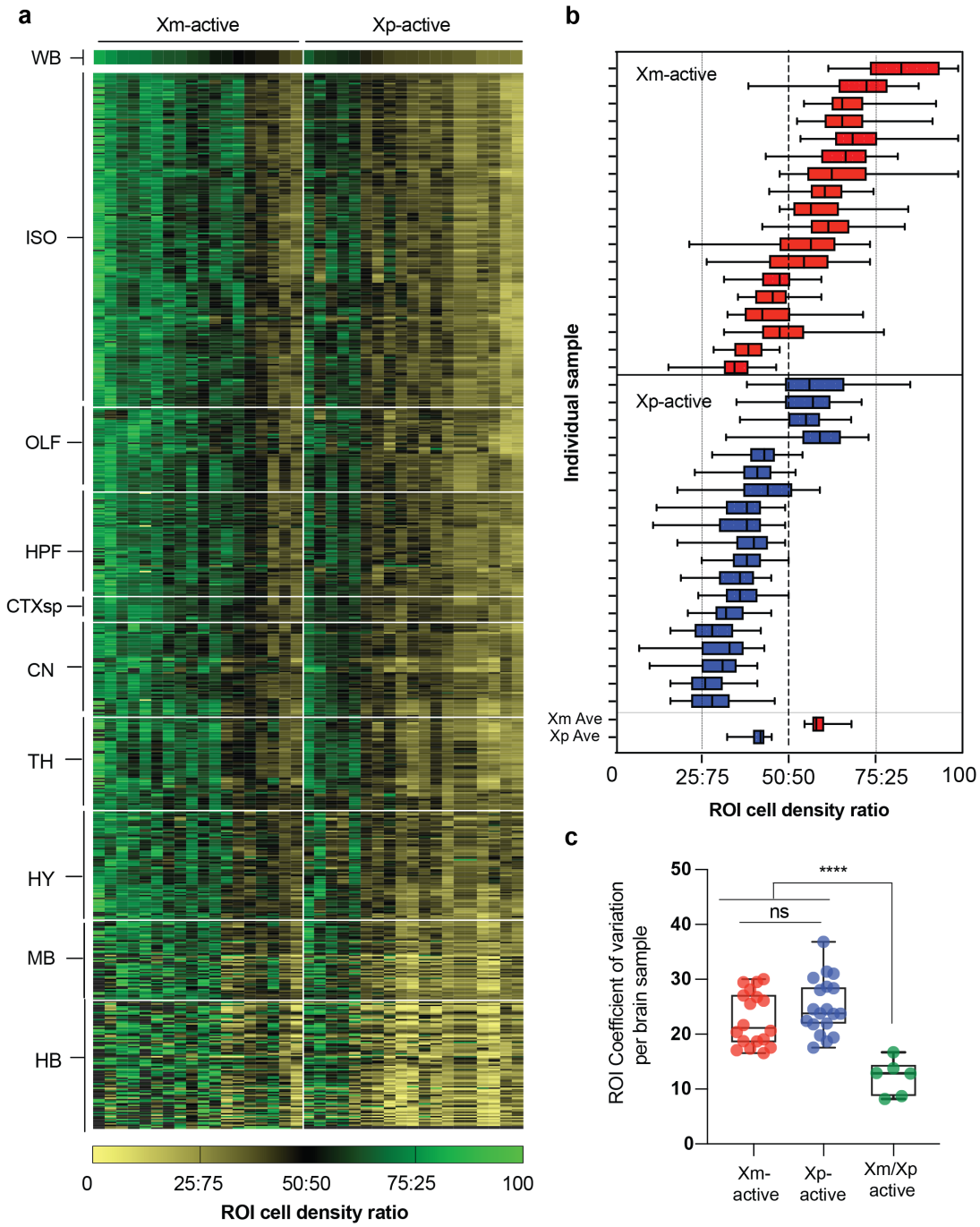

759

760 **Fig. 2 | Quantification of Xm and Xp selection and its variability across all brain**
761 **regions. a**, 2D heatmap of brain-wide ROI cell density ratios in which each column
762 represents one animal from maternal Mecp2-GFP(m/+) (left) and paternal Mecp2-
763 GFP(p/+) (right) reporter brains. The Xm and Xp selection is expressed
764 asmeasured:estimated cell density ratios across all 738 brain ROIs and displayed on a color
765 gradient of beige to black (0 to 50:50), and black to green (50:50 to 100%). The samples

are ordered from high (left) to low (right) XCI selection for each genetic group on the x axis whereby the ROIs are ordered by major ontological division along the y-axis. **b**, Stochastic variability of Xm versus Xp selection across all brain regions in each brain analyzed. The average data for Xm-GFP and Xp-GFP brains is plotted at the bottom. Box-and-whisker plots display median, interquartile range, and 95th percentiles of the data. **c**, Quantification of brain-wide ROI stochastic variability for Xm-GFP versus Xp-GFP versus homozygous Xm-GFP/Xp-GFP alleles by coefficient of variation analysis (CV): mean ± SD = 22.8 ± 4.9 vs 25.08 ± 5.1 vs 12.16 ± 3.2. ***$p<0.005$ from 1-way ANOVA with Dunnet's post-hoc corrected multiple comparisons.; 25% percentile = 18.41 vs 21.79 vs 8.56, Median = 21.14 vs 23.78 vs 12.83, 75% percentile = 27.31 vs 28.68 vs 14.48.

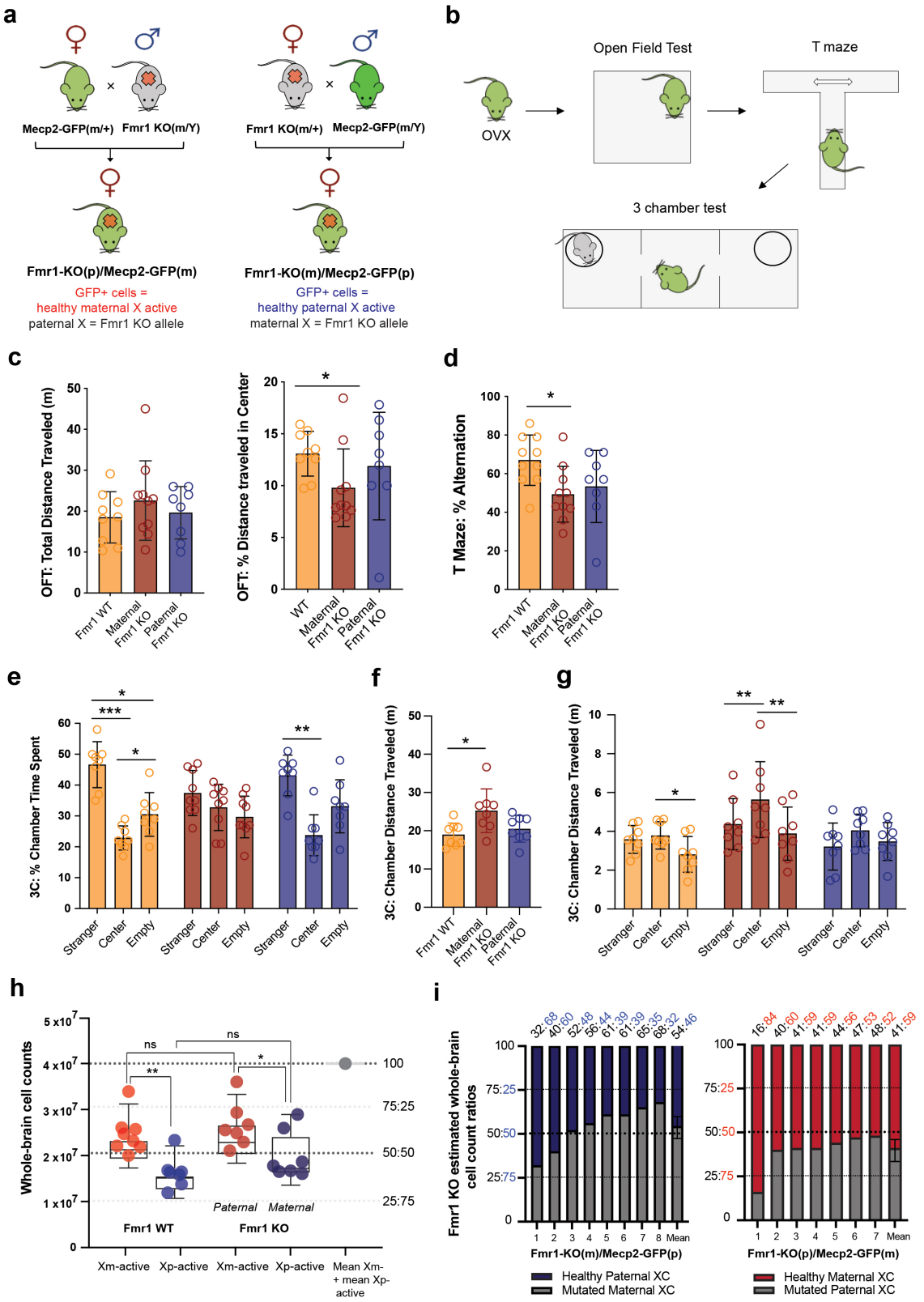

794 **Fig. 3 | Maternal transmission of the Fmr1-KO allele at an average 46:54 Fmr1-**
795 **WT:KO cell ratio is sufficient for phenotypic penetrance. a**, The Fmr1 KO allele was

796 transmitted either maternally in Fmr1-KO(m)/Mecp2-GFP(p) mice (in figures for short
797 Fmr1-KO(m)/+; left) or paternally in Fmr1-KO(p)/Mecp2-GFP(m) mice (in figures Fmr1-
798 KO(p)/+; right) by breeding with Mecp2-GFP male or female mice, respectively. **b**,
799 Behavioral testing: ovariectomized (OVX) heterozygous maternal Fmr1-KO(m)/+,
800 paternal Fmr1-KO(p)/+ and WT littermate mice were sequentially tested in the open field
801 test (OFT), T maze, and 3-chamber social test (n=8 for each group). Data for each
802 individual test are derived from sequential data of the same animals. **c**, OFT results show
803 reduced exploration only in maternal Fmr1-KO(m/+) mice: Left: Total distance traveled
804 was not different among the three groups (mean ± SD; meters): WT: 19.2 ± 6.3; Fmr1-
805 KO(m/+): 23.2 ± 10.6; Fmr1-KO(+/p): 19.6 ± 6.3. Right: Percent distance traveled in
806 center arena was reduced in Fmr1-KO(m)/+ mice (mean ± SD): WT: 13 ± 2; KO(m/+): 9
807 ± 3; KO(+/p): 12 ± 5. ANOVA, K-W = 6.47; p = 0.039; Welch's ANOVA and Dunnet T3
808 post-hoc test: WT vs Fmr1-KO(m/+): p = 0.035. **d**, T maze results show reduced working
809 memory, seen in reduced percent spatial alterations, only in maternal Fmr1-KO(m/+) mice
810 (mean ± SD): WT: 69 ± 14; Fmr1-KO(m/+): 47 ± 15; Fmr1-KO(+/p): 53 ± 19. Welch's
811 ANOVA, Dunnet T3 post-hoc comparisons: WT vs Fmr1-KO(m/+): p = 0.023. **e**-**g**, 3-
812 chamber test identifies deficits only in maternal Fmr1-KO(m/+) mice. **e**, Fmr1-KO(m)/+
813 show a lack of sociability in the 3-chamber test. Time spent for the 3 genotypes in social
814 vs center vs empty chamber were (mean ± SD): WT = 47 ± 7 vs 23 ± 4 vs 31 ± 7; Fmr1-
815 KO(m/+) = 39 ± 6 vs 32 ± 8 vs 29 ± 7; Fmr1-KO(+/p) = 43 ± 7 vs 24 ± 7 vs 33 ± 9; 2-way
816 mixed effects ANOVA, Holm-Sidak post-hoc comparisons; *p<0.05; **p<0.01;
817 ***p<0.001. **f**, Fmr1-KO(m)/+ mice were hyperactive compared to WT mice as seen in
818 increased total distance traveled (mean ± SD): 24.25 ± 6.10, 18.96 ± 3.07 and 20.49 ± 3.48,
819 respectively. Welch's ANOVA and Dunnet T3 post-hoc comparisons, WT vs Fmr1-
820 KO(m/+): p = 0.037. **g**, The hyperactivity of the Fmr1-KO(m)/+ mice was restricted to the
821 starting central arena of the 3-chamber apparatus. Distance traveled for the 3 genotypes in
822 social vs center vs empty chamber were (mean ± SD): WT = vs 3.79 ± 0.71 vs 3.08 ± 1.17;
823 Fmr1-KO(m)/+ = 4.37 ± 1.32 vs 5.63 ± 1.96 vs 3.80 ± 1.36; Fmr1-KO(p)/+ = 3.22 ± 1.21
824 vs 4.05 ± 0.84 vs 3.71 ± 0.98; *p<.05; **p<.01, 2-way mixed effects ANOVA, Holm-Sidak
825 post-hoc comparisons. **h**, Quantification of whole-brain Xm vs Xp selection in WT mice

826 (left) and heterozygous Fmr1 KO mice (right) (mean ± SD): WT: Xm-active cells = 2.6 x
827 $10^7 \pm 4.7 \times 10^6$ and Xp-active cells = $1.7 \times 10^7 \pm 3.6 \times 10^6$; maternal KO allele in Fmr1-
828 KO(m/+): healthy Xp-active cells in = $2.0 \times 10^7 \pm 5.2$ and paternal KO allele in Fmr1-
829 KO(p/+): healthy Xm-active cells = $2.6 \times 10^7 \pm 4.8$. *$p<0.05$, **$p<0.01$, ANOVA with
830 Holm-Sidak post-hoc comparisons. Estimated 75:25 and 25:75 whole-brain cell count
831 ratios are shown in dashed lines. **i**, Stacked bar graphs of each maternal Fmr1-KO(m/+)
832 (left) and paternal Fmr1-KO(+/p) (right) whole-brain X selection from (**h**): healthy Xp-
833 active cells in Fmr1-KO(m)/+ brains are highlighted in dark blue color (left) and healthy
834 Xm-active cells in Fmr1-KO(p/+) are highlighted in red color (right). Fmr1-KO:WT
835 cellular ratios of each sample is listed above.
836
837

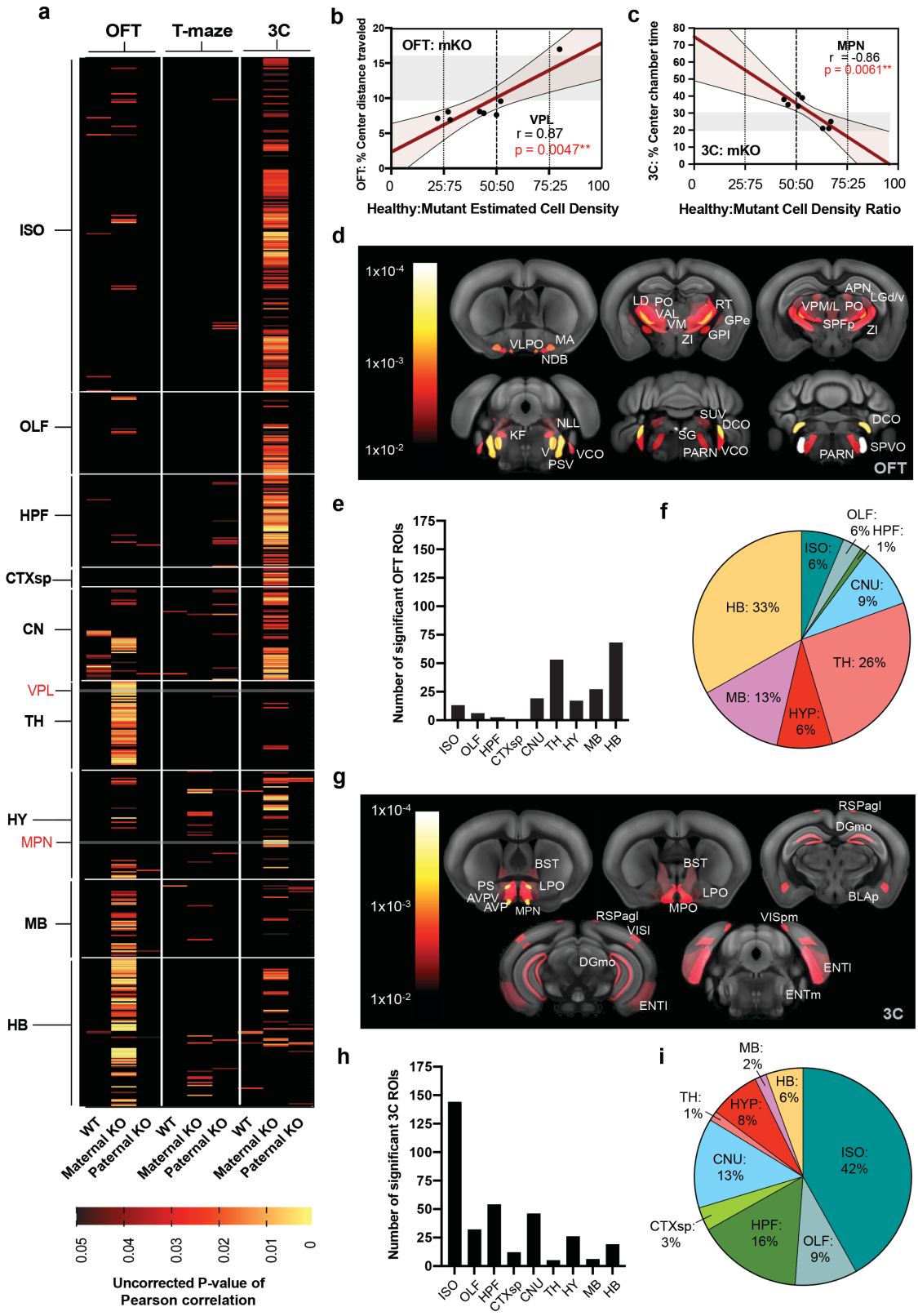

Figure 4 | Identification of two sets of brain regions with local Fmr1-WT:KO cell

840 **ratios linked to phenotypes in the OFT and 3-chamber test. a**, Identified brain regions
841 in Fmr1-KO(m)/Mecp2-GFP(p) ("Maternal KO") mice that correlate Fmr1 WT:KO allele
842 ratios to behavioral performance in the OFT and 3-chamber tests. Data are displayed as 2D
843 heat maps of statistically significant correlations across brain ROIs grouped by major
844 ontological structures. Uncorrected P values of Pearson correlations are represented on a
845 color gradient scale from 0.05 (black) to 0.005 (red) to 0.0005 (yellow). Results from Fmr1
846 WT ("WT"), maternal Fmr1-KO(m)/Mecp2-GFP(p) ("Maternal KO") and paternal Fmr1-
847 KO(p)/Mecp2-GFP(m) ("Paternal KO") mice are grouped by each behavioral test: left:
848 OFT, center: T maze, right: 3-chamber (3C). **b-c**, Representative scatterplot displays of
849 correlated ROI density from (**a**) shown for (**b**) VPL of thalamus in OFT and (**c**) MPN of
850 hypothalamus in 3 chamber tests. **d**, **g**, Selected ROIs from maternal Fmr1-KO(m)/Mecp2-
851 GFP(p)\ mice with significant correlation (cut-off at p=0.01) to performance in (**d**) OFT
852 and (**g**) 3 chamber tests are heat mapped and overlaid on a reference mouse brain template.
853 **e**, **h**, Number of significantly correlated ROIs from maternal Fmr1-KO(m)/Mecp2-GFP(p)
854 mice listed by major brain structure for (**e**) OFT and (**h**) 3 chamber tests. **f**, **i**, 100% pie
855 charts of significantly correlated ROIs from maternal Fmr1-KO(m)/Mecp2-GFP(p) mice
856 grouped by major brain structure and represented as a percent of total correlated ROIs for
857 (**f**) OFT and (**g**) 3-chamber test. ROI acronyms: VLPO – ventrolateral preoptic area; NDB
858 – nucleus of the diagonal band; MA – magnocellular nucleus; PO – posterior complex of
859 the thalamus; VPM/L – ventral posteromedial/lateral nucleus of the thalamus; PC –
860 paracentral nucleus; RT – reticular nucleus of the thalamus; ZI – zona incerta; GPi – globus
861 pallidus, internal; GPe – globus pallidus, external; SPFp – subparafacsicular nucleus,
862 parvicellular part; LGv – ventral part of the lateral geniculate nucleus; LGd – dorsal part
863 of the lateral geniculate nucleus; KF – Koelliker-Fuse subnucleus; V – motor nucleus of
864 the trigeminal; PSV – principal sensory nucleus of the trigeminal; VCO – ventral cochlear
865 nucleus; SG – supragenual nucleus; DCO – dorsal cochlear nucleus; VCO – ventral
866 cochlear nucleus; SPVO – spinal nucleus of the trigeminal, oral part, E, F) PS – parastrial
867 nucleus; BST – bed nuclei of the stria terminalis; AVP – anteroventral preoptic nucleus;
868 AVPV – anteroventral periventricular nucleus; MPO – medial preoptic nucleus; LPO –
869 lateral preoptic area; RSPAgl – retrosplenial cortex, agranular layer; DGmo – dentate

gyrus, molecular layer; BLAp – basolateral amygdala, posterior; VISpm – posteromedial visual area; VISl lateral visual area; ENTl – entorhinal area, lateral; ENTm – entorhinal area, medial.

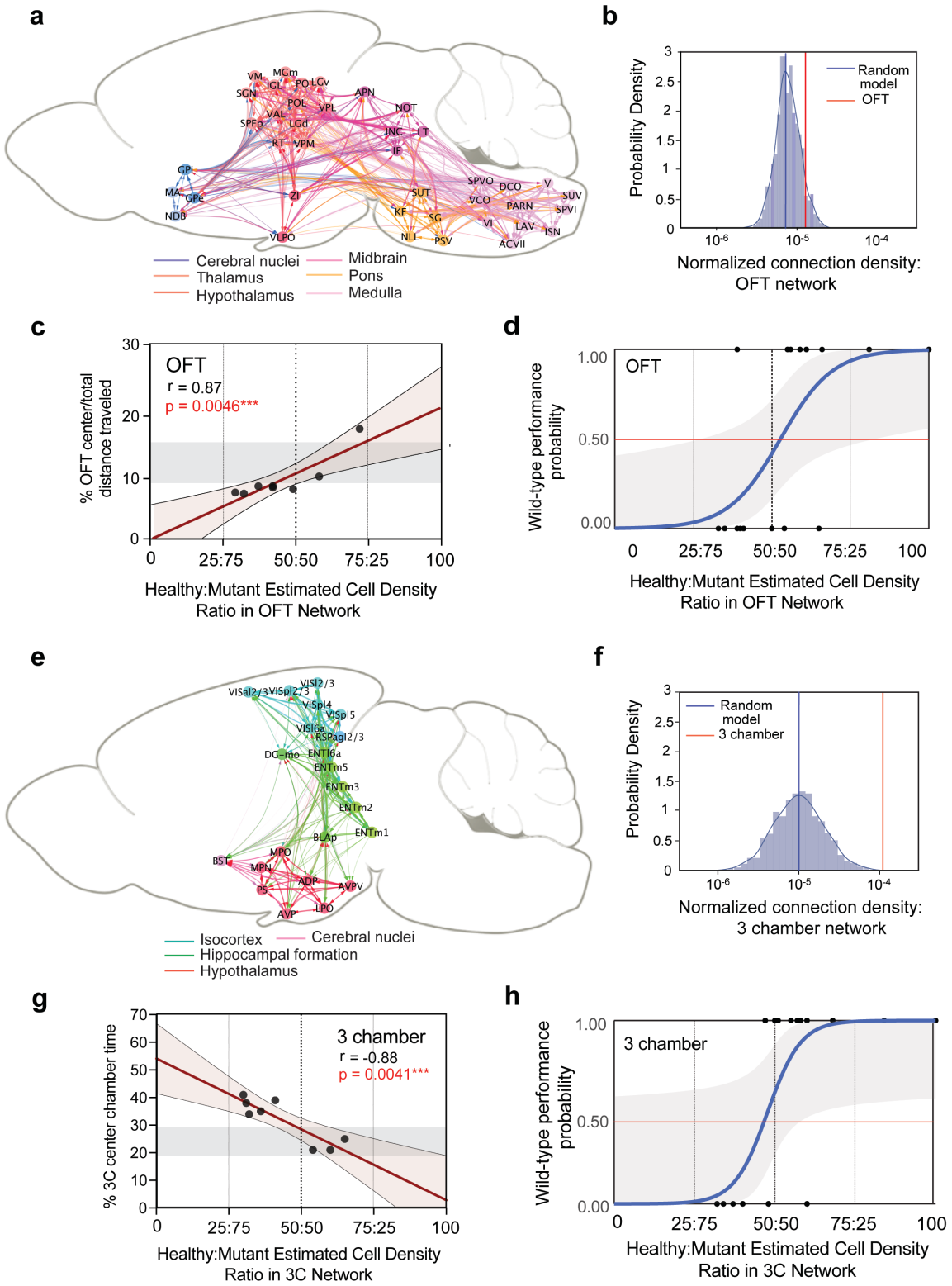

Fig. 5 | FXS phenotypic penetrance in the OFT and 3-chamber tests is determined by XCI-defined healthy:mutant cellular ratios within structural brain networks. a, e,

877 Visualization of structural connectivity weights within brain networks of ROIs with
878 WT:KO allele ratios correlated to behavioral performance in the (**a**) OFT and (**e**) 3-
879 chamber tests (See Methods). **b**, **f**, Normalized median connection densities of the (**b**)
880 OFT ($1.22e^{-6}$) and (**f**) 3-chamber ($9.95e^{-4}$) ROI networks (red lines) overlaid on the
881 probability density of 1000 in-silico generated random ROI networks of the same inter-
882 regional distance and ROI amount (blue line = median; OFT: 7.22×10^{-6}; 3 chamber: 9.95
883 $\times 10^{-6}$). One sample t test: OFT: $p = 6.36 \times 20^{-247}$; 3-chamber: $p = 0.0$). Data is compared
884 and presented on a log scale. **c**, **g**, Linear regression models of behavioral scores and ROI
885 network cell density ratios in (**c**) OFT and (**g**) 3-chamber assays. Regression and statistical
886 test values are listed for each panel. Shadowed rectangle in each group represents
887 control Fmr1 WT range of behavioral scores for comparison. **d**, **h**, Logistic regression
888 modeling of WT behavioral performance predicted by healthy cell density percent in ROI
889 networks of behavioral penetrance from all mice (n=22) within (**d**) OFT (K; $x^2(1) = 14.88$;
890 log-likelihood ratio = -14.42; equal odd ratio = 54%; $p = 0.00011$) and (**h**) 3 chamber (L;
891 $x^2(1) = 13.88$; log-likelihood ratio = -12.89; equal odd ratio = 49%; $p = 0.00019$) behaviors.
892 Grayed area represents ± 95% confidence intervals.
893
894
895
896
897
898
899
900
901
902
903
904
905
906
907
908
909
910
911
912

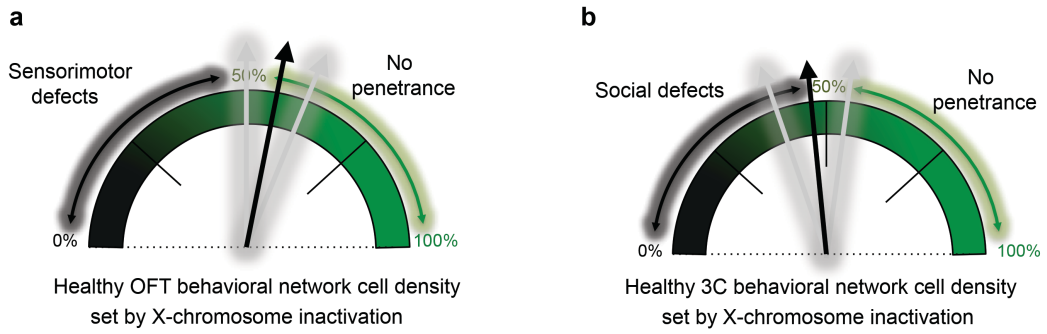

Fig. 6 | Cartoon depiction model of (**a**) OFT and (**b**) 3 chamber logistic modeling results (Fig 5), which portrays how female FXS phenotypes are determined by the distributed healthy cell density occupying the ROI behavioral networks identified in this study.

949 **Methods**

950

951 **Animal breeding and husbandry.** Adult mice (8-10 weeks old) were used for whole-
952 brain imaging experiments. Animals were housed under a 12-hour light/dark cycle (0600
953 ON, 1800 OFF), had access to food and water ad libitum, and were housed with littermates.
954 All experimental procedures were performed in accordance with CSHL Animal Care and
955 Use Committee Guidelines. The Mecp2-GFP mouse line was obtained from the Jackson
956 laboratory (stock # 014610). Mecp2 is a gene located at chromosomal position X A7.3 and
957 is subject to XCI. Developed in the laboratory of Adrian Bird, this mouse line contains an
958 in-frame knock-in cassette at the 3' UTR of the Mecp2 locus [46,47,93,94]. Driven and regulated
959 by the endogenous Mecp2 promoter/enhancers, Mecp2-GFP expression leads to normal
960 Mecp2 levels and subcellular localization of Mecp2 protein that is fused at the C-terminus
961 with EGFP. Expression of the fusion allele does not alter neuronal physiology [94] and mice
962 are successfully bred to homozygosity without behavioral or reproductive complications
963 (data not shown). In addition, strong expression of Mecp2-GFP favors neurons of many
964 types [46] thereby circumventing biased effects of XCI determinations based on expression
965 profile. Mecp2-GFP(m/+) or Mecp2-GFP(p/+) mice were obtained in separate
966 heterozygotes by crossing homozygous females or hemizygous males with wild-type
967 C57Bl6/J (JAX stock # 000664) mice. A subset of these wild type reporter mice was
968 derived from Fmr1 KO or WT crosses that generated Mecp2-GFP(m/+)/Fmr1
969 KO(+/+) (n=7) and Mecp2-GFP(+/p)/Fmr1 KO(+/+) (n=8) mice that are congenic to the
970 C57Bl6/J crosses. Homozygous reporter mice were obtained by
971 crossing homozygous Mecp2-GFP(m/p) females with hemizygous Mecp2-
972 GFP(m/Y) males. Fmr1 KO mice were obtained from the Jackson laboratory (#003025).
973 These mice were originally developed in the Oostra laboratory and contain a gene-
974 disrupting neomycin resistance cassette in exon 5 of the FMR1 locus [51]. Mecp2-
975 GFP(m/+)/Fmr1 KO(+/p) female mice were generated by breeding Mecp2-
976 GFP(m/p) females with hemizygous Fmr1 KO(m/Y) males. For imaging only, Mecp2-
977 GFP(m/+)/Fmr1 KO(+/+) female mice were generated by separately breeding
978 homozygous Mecp2-GFP(m/p) females with hemizygous Fmr1 KO(+/Y) males.
979 Conversely, Mecp2-GFP(+/p)/Fmr1 KO(m/+) or Mecp2-GFP(+/p)/Fmr1 KO(+/+) wild

980 type littermates were generated by breeding Fmr1 KO(m/+) females with
981 hemizygous Mecp2-GFP(m/Y) males. Using this genetic strategy, double heterozygous
982 mice used for behavior and imaging experiments contained the Mecp2-GFP and Fmr1 KO
983 alleles on opposing X chromosomes. All transgenic mice were maintained on a C57Bl6/J
984 background.
985
986 **Brain sample preparation.** Animals were euthanized via transcardial perfusion under
987 ketamine/dexmedetomidine anesthesia. Dissected brains were post-fixed overnight in 4%
988 paraformaldehyde at 4 C, incubated for 48 h in 0.1 M glycine/0.1 M PB for auto fluorescent
989 quenching, and then stored in 0.05 M PB at 4 C until confocal or serial two-photon
990 tomography imaging (STPT; see below). Prior to STPT imaging, brains were embedded
991 4% oxidized agarose in 0.05 M PB using custom molds and holders to maintain consistent
992 embedding position. Embedded brains were crosslinked in 0.2% sodium borohydrate
993 solution for 3h at room temperature or overnight at 4 C prior to STPT processing (below).
994
995 **Immunohistochemistry and confocal imaging.** Neuronal expression of the MeCP2-GFP
996 allele was studied though immunostaining and confocal imaging. 50 um vibratome-
997 processed, free-floating coronal sections of homozygous MeCP2-GFP mice brains (n=2)
998 were processed. Sections were washed 3 times in PBS followed by blocking for 1 h at room
999 temperature in PBS- T (PBS, 0.2% Triton-X 100) containing 5% donkey serum. Sections
1000 were then incubated overnight at 4 C in blocking solution containing rabbit anti-NeuN
1001 (Millipore, ABN78) primary antibody at 1:1000. After washing, NeuN-stained sections
1002 were incubated with anti-rabbit AlexaFluor-568-conjugated secondary antibody (Thermo-
1003 Scientific, A10042) diluted 1:500 for 1 h at room temperature. After washing excess
1004 secondary antibody, sections were mounted, DAPI- counterstained (Prolong Gold Antifade
1005 Mountant, Thermo Fisher), and coverslipped for imaging. Confocal images were acquired
1006 with a Zeiss LSM780 confocal microscope using a 561 laser and corresponding dichroic
1007 and filter sets. Single plane images were captured with a 40x oil immersion objective. Total
1008 colocalized populations for each marker of every FOV (212.55 um X x 212.55 um Y) were
1009 manually quantified using Fiji image processing package.
1010

1011 **Serial two-photon tomography whole-brain image acquisition**. The Tissuecyte1000
1012 instrument was used for all imaging experiments (TissueVision) [44]. This system combines
1013 a high-speed multi- photon microscope with a fully integrated vibratome for automated z-
1014 sectioning and image acquisition throughout the entire whole-mount sample. Embedded
1015 sample brains were imaged with a 20x objective at 50 μM below the sample surface. 270
1016 total serial sections were acquired at 50 um z-resolution (13.5 mm total z-length), with each
1017 section being comprised of a 12 (x-axis, 700 um) x 16 (y-axis, 700 um) field of view (FOV)
1018 mosaic. Images were acquired with laser scan settings of 1 um/pixel at an integration time
1019 of 1 us. A laser wavelength of 910 nm with ~322 mW power at the end of the objective
1020 was used for optimal excitation/emission of MeCP2-GFP fluorescence. Constant laser
1021 settings and PMT detector settings were used for all samples.
1022
1023 **Automated MeCP2-GFP+ cellular detection and counting.** Raw image tiles for each
1024 brain were illumination corrected, stitched in 2D with Matlab and aligned in 3D using Fiji
1025 software [44]. For reliable automated MeCP2-GFP detection from full brain datasets, we
1026 implemented convolutional networks (CNs) [95]. CN training for detection of MeCP2-GFP+
1027 cells in the STPT datasets was accomplished as in previous studies [43] with CN training
1028 performed on human marked-up ground truth data (biological expert identified MeCP2-
1029 GFP+ nuclei) of MeCP2-GFP brains. CN performance was determined based on F-score
1030 calculations (F-score = the harmonic mean of the precision and recall, where precision is
1031 the ratio of correctly predicted cells divided by all predicted cells and recall is ratio of
1032 correctly predicted cells divided by ground truth positive cells; ~1800 MeCP2-GFP+ cells
1033 were marked/expert/brain). Composite F-scores for MeCP2-GFP CN was obtained by
1034 determining F-scores in 8 FOVs (400 (X) um by 400 (Y) um) representing different cellular
1035 density and imaging content in 3 separate heterozygous MeCP2-GFP+ brains (24 FOVs
1036 total). Stable precision and recall was seen for all regions analyzed, delivering a composite
1037 F-score of 0.84 (Extended data Fig. 2). In the CN output images, signal smaller than 10
1038 μm^2 was removed as noise. In order to normalize the performance of CN for each brain,
1039 the brightness of MeCP2-GFP+ signal for each sample was normalized by the mean and
1040 standard deviation of tissue autofluorescence signal from a coronal section corresponding

1041 to bregma position of +0.20 mm. We did not analyze MeCP2-GFP+ cells in the cerebellum
1042 due to faulty brain-to-brain warping of this region (data not shown).
1043
1044 **3D brain registration and anatomical segmentation.** Registration of individual brains to
1045 a standardized reference space was computationally achieved as published previously [43].
1046 In short, affine transform was calculated using 4 resolution levels and B-spline with 3.
1047 Advanced Mattes mutual information [96] was the metric used to measure similarity between
1048 moving and fixed images. Image similarity function is estimated and minimized for a set
1049 of randomly chosen samples with each 23 images in a multi-resolution and iterative fashion
1050 [44]. Entire warping of whole-brain images is done using Elastix [97]. Anatomical segmentation
1051 of Allen Brain Atlas (ABA) labels onto sample brains was made possible also as previously
1052 published [43]. Version 2.2 ABA labels (836 total) were transformed onto individually
1053 registered samples. Quality control of ROI segmentation found and excluded 95 ROIs total
1054 from analysis due to erroneous counting most likely caused by small ROI size and/or
1055 warping location (Full ROI list found in Supplementary Table 1). In addition, cell counts
1056 from layer 6 a and b were combined into one layer, layer a.
1057
1058 **2D-3D cell count correction and density measurements.** Detected 2D cell count values
1059 obtained at 50 um Z resolution were transformed by a stereological 3D conversion factor
1060 obtained by the following way (Extended data Fig. 2). First, counting boxes of 200 um x
1061 200 um x 50 um (xyz) were acquired at 2.5 um Z resolution via optical imaging within 6
1062 brain regions comprising major anatomical divisions of a female heterozygous MeCP2-
1063 GFP mouse brain. 20 optical images were acquired at a depth range that spanned 50 um
1064 around the normal 50 um focal depth (i.e. 25-75 um below the tissue surface). Second,
1065 Mecp2-GFP CN was run on the middle optical section corresponding to the 50 um depth.
1066 Third, manual markup of Mecp2-GFP+ nuclei was performed in each counting box using
1067 the stereological counting rules of Williams and Rakic [98]. Lastly, a conversion factor for
1068 each region was calculated by dividing manual 3D counts by 2D CN count of the middle
1069 section. This factor was averaged over the 6 regions reaching a final conversion factor of
1070 2.6. (Extended data Fig. 2b). ROI cellular density was obtained by 1) transforming ABA

1071 labels onto individual brains, 2) converting ROI assigned pixel space to mm^3, 3) dividing
1072 2.5 um Z-corrected absolute cell counts by mm^3 values by to arrive at cells/mm3.
1073
1074 **Behavioral testing.** 6-8 month old ovariectomized female mice were behaviorally
1075 phenotyped in a sequential series of tests. All mice were ovariectomized at least 2 weeks
1076 prior to testing in order to remove estrous cycle influences from behavior. Each behavioral
1077 test was separated by 2-7 days to avoid acute post-testing and handling effects. Mecp2-
1078 GFP(+/p)/Fmr1 KO(+/+) mice served as behavioral controls for all behaviors studied. The
1079 following tests were sequentially performed on each mouse:
1080
1081 *Open field test (OFT).* To measure activity and anxiety in an open field, unhabituated mice
1082 were placed in a 40 x 40 x 40 cm2 open plexiglass box containing a layer of fresh bedding.
1083 The open field arena was located in a non-sound-proof, enclosed environment under dim
1084 lighting. All mice were housed in the same facility room behavioral testing was performed.
1085 An overhead camera visually captured all tests and ANY-maze (Stoelting) automated
1086 behavior tracking software was used for real-time activity/location recording and analysis.
1087 A 20 x 20 cm center square designated within the tracking settings defined the center and
1088 perimeter boundaries of the arena. The software measured total and center distance
1089 traveled. For center-specific activity, center distance was normalized to total distance
1090 traveled and presented as percent total distance traveled. Adequate cleaning of the maze
1091 with bleach, water and drying was performed between each mouse. Fresh bedding was
1092 added to the arena for each subject.
1093
1094 *T-maze*. We studied mouse spatial memory by measuring spontaneous spatial alternations
1095 in the T-maze [99,100]. Spontaneous alternation is an innate exploratory behavior possessed by
1096 rodents which is hippocampus-dependent and serves as an index of spatial and working
1097 memory [99]. Our protocol was based off of the continuous version with minor modification
1098 [100]. The dimensions of the T-maze used was 35 cm stem length, 28 cm arm length, 10 cm
1099 arm height, and 5 cm lane width (Stoelting). For testing, the T-maze was located in a non-
1100 sound-proof, enclosed environment under dim lighting. All mice were housed in the same
1101 facility room behavioral testing was performed in. To begin the test, each mouse was

1102 carefully placed at the stem start position of the maze and was freely allowed to enter either
1103 arm. To prevent the mouse from entering the other arm after its initial choice, a metal block
1104 was placed at the entrance of the empty arm once the subject committed exploration to an
1105 arm. The subjects were allowed to freely explore the chosen arm and stem until it explored
1106 back to start of the stem. Once the beginning position was reached, the mouse was held in-
1107 between the start position and a metal block placed proximally to the start position for 5
1108 seconds. The metal block was then removed and the mouse was allowed again to enter an
1109 arm of its choice. Manual scoring of each arm choice and time to experimental completion
1110 was made after 14 trials. No more than 3 minutes/trial was allowed for each subject and
1111 encouragement was given to each subject at 3 minutes (in the form of hand movement
1112 behind the mouse) to return to start position. Mice that did not complete more than 9 trials
1113 were excluded from analysis. Adequate cleaning of the maze with bleach, water and drying
1114 was performed between each mouse. The number of trial-to-trial arm entry alternations
1115 (e.g. left-to-right or right-to-left) was calculated and expressed as a percent of total trials.
1116
1117 *3-chamber test*. Sociability was measured using the 3-chamber test based on the protocol
1118 developed in the Crawley laboratory[102]. The 3-chamber apparatus used consisted of a
1119 plexiglass box (60 x 40 x 22(h) cm) partitioned into 3 chambers (20 cm/each) (Stoelting).
1120 Doors (4 x 8 cm) connecting chambers allowed the mice to freely explore all areas of the
1121 box. The apparatus was located in a non-sound-proof, enclosed environment under dim
1122 lighting. All mice were housed in the same facility room that behavioral testing was
1123 performed in. An overhead camera visually captured all test sessions and ANY-maze
1124 (Stoelting) automated behavior tracking software was used for real-time activity/location
1125 recording and analysis. Chamber designations in tracking software were user-defined and
1126 used for chamber-specific activity measurements. Two metal-barred cylindrical cages (7
1127 cm (diameter) x 15 cm (height); 3 mm bar diameter and 7 mm spacing) were used for
1128 stranger mouse containment in one chamber and for an empty enclosure in the opposite-
1129 sided chamber. The cage bars are spaced such that close sniffing is the only interaction
1130 type possible. Ovariectomized adult female Fmr1 WT mice were used as stranger mice and
1131 were habituated to an enclosure cage for 10 minutes at least 1 day prior to any experiments.
1132 Each stranger mouse (n=8) was used 4 times only and were rotated every 4 experiments

1133 for use. Test mice were habituated to an empty 3 chamber apparatus for 10 minutes prior
1134 to actual experiments. For testing, mice were allowed to freely explore all chambers for 10
1135 minutes. For each experiment the enclosed stranger mouse was placed in the left chamber
1136 and the empty enclosure on the right. Chamber time spent and distance traveled was
1137 quantified for each chamber. Percent time spent or distance traveled was calculated as total
1138 value/individual chamber value.
1139

1140 **Quantification of structural connectivity within correlated brain networks of ROIs.**
1141 We determined if OFT and 3-chamber significantly correlated ROI groups (herein referred
1142 to as "networks") represented structural connectivity networks by comparing the median
1143 ROI network connection weight to a distribution of randomly sampled networks of the
1144 same size for both tasks. ROIs having significant correlation of $p<0.01$ were included in
1145 the analysis. We used the normalized connection density, a measure of connection strength
1146 normalized by both source and target region sizes, from the regional structural connectivity
1147 matrix [66]. We restricted the population of structures for each network to ROIs from which
1148 we could draw to an intermediate level of the ontology represented by 292 'summary
1149 structures' [101]. The intersection of these summary structures with the sets of ROIs for each
1150 task resulted in sets of 39 and 13 ROIs for the open field and 3-chamber tasks,
1151 respectively (**Table S6**). These ROIs included: OFT: ACVII, APN, DCO, GPe, GPi, IF,
1152 IGL, ISN, LAV, LGd, LGv, LT, MA, MG, NDB, NLL, NOT, PARN, PB, PO, POL, PSV,
1153 RT, SG, SGN, SPFp, SPVI, SPVO, SUT, SUV, V, VAL, VCO, VI, VLPO, VM, VPL,
1154 VPM, ZI; 3 chamber: ADP, AVP, AVPV, BST, ENTl, ENTm, LC, LPO, MPN, MPO, PS,
1155 VISl, VISpl. Additionally, since mesoscale connectivity is distance dependent [101] and the
1156 model in [66] is spatially dependent, we restricted the selection of random ROI networks to
1157 have similar inter-regional distance dependence as that of their respective cell density
1158 correlated ROI networks.
1159 The procedure for this selection is as follows:
1160 Given a set of N cell density correlated summary structure level ROIs:
1161 1) Randomly draw a set of N regions from the set of summary structures.
1162 2) Compute the pairwise inter-regional distances for the set of sampled regions.

1163 3) Compute the Kolmogorov-Smirnov statistic to measure the difference in distributions
1164 of distances for the sampled and cell-count correlated networks
1165 a) If the KS statistic shows a significant difference in distributions (having a p-value <
1166 0.01), reject the sample and return to (1).
1167 b) Else, return the sample.
1168 The above procedure is repeated 1000 times, after which the median normalized connection
1169 density of the experimental ROI networks is compared to the distribution of the sample
1170 medians. Since these connectivity measures are log-normally distributed [66,101] the t statistic
1171 is computed in log-transformed space to test the significance of the difference.
1172 Visualization of ROI-ROI connectivity for each behavioral network of ROIs was created
1173 with Cytoscape network visualization and analytic program (Version 3.7.1). Significantly
1174 correlated ROIs of the deepest ontological distance from root structures were chosen for
1175 visualization, except for the ROIs not annotated at the summary structure level and hence
1176 not found in the structural connectivity matrix. Those ROIs
1177 included: BSTmg, BSTpr, BSTif, BSTpr, PVHap, TTv3, isl, islm, MPNc, MPNl, PAA3,
1178 and COApl3. Log-transformed normalized connection densities were used for edge
1179 sizes and scaled for presentation. Edges with sizes < 0 were excluded from the
1180 visualization.
1181
1182 **Statistics.** Whole-brain absolute cell counts were compared amongst Xm-active and Xp-
1183 active reporter brains using a Welch's t test. A 2-way mixed effects ANOVA ([2] XC-
1184 active/KO or WT allele parent-of-origin x [9] major ROI) was used to compare XC-active
1185 (Fig. 1) or WT:KO allele (Fig. 2) parent-of-origin across cell densities from major ROIs.
1186 Holm-Sidak post-hoc tests were used to assess simple between-subjects effects. Brain-
1187 wide screens for skewed XCI were statistically performed using Benjamini-
1188 Hochberg FDR-corrected student's t tests on XC-active cell density groups. Welch's
1189 ANOVAs with Dunnet's T3 post-hoc testing was used to compare group performances in
1190 the OFT, T maze, and 3 chamber total distance traveled. Chamber by group 3 chamber
1191 results were analyzed with 2-way mixed effects ANOVAs with Holm-Sidak post-hoc tests
1192 of between- and/or within-subjects simple effects. Whole-brain absolute healthy cell
1193 counts in Fmr1 WT and KO mice were analyzed via ANOVA with Holm-Sidak post-hoc

comparisons. Whole-brain cell count data and behavioral scores were correlated with Pearson's correlation. Correlational screens were used to localize the physical source of behavioral penetrance using Pearson's correlation amongst cell density and behavioral score across 736 ROIs. In this analysis, we did not correct the p-values against Type I error risk in favor of revealing ROI networks or patterns that share behavioral dependencies. Additionally, noise correlations (Supplementary Table 5) in the control WT groups did not surpass 5% of ROIs in both OFT (20/736 ROIs = 2.7%) and 3 chamber (5/736 ROIs = 0.6%) screens, further supporting the use of uncorrected p values in this dataset. ROI networks of behavioral penetrance were defined by $p<0.01$ bins of significance and each bin's distributed cell count, volume, and density across each OFT and 3 chamber networks were calculated (Supplementary Table 7) and used for linear and logistic regression modeling. Logistic regression was performed on ROI network healthy cell density percent as the continuous, independent variable and WT performance as the categorical, dependent variable. Mice (n=22) from all genotypes were categorized as WT or mutant performers for each test based on the performance range of Fmr1 WT mice. Fmr1 WT mice were coded as containing 100% healthy cell density. A likelihood ratio test was performed on each logistic model to determine statistical significance. All statistical testing was performed with Graphpad Prism software version 7.0 and R (R Core Team). Alpha level was set at 0.05 in all analyses except where otherwise noted above.

Acknowledgements

We would like to thank CSHL Hillside animal husbandry services for their support and efforts, members of the Osten lab for inputs on the study and Dr. Kristin Baldwin for comments on the manuscript. This work was funded by grants R01 MH096946 and U01 MH105971 to P.O and funds from The Gertrude and Louis Feil Family Trust to PO.

Author Contributions

E.R.S. and P.O. conceptualized the study. E.R.S., P.O., and Y.K. designed the imaging experiments. R.P. performed genotyping and animal husbandry and assisted with experimental design. E.R.S. and K.U.V. implemented CN algorithms for automated cell

detection. E.R.S. designed and D.F. performed all behavioral experiments. E.R.S. performed tissue processing and imaging experiments and most data analyses. J.K. and J.A.H. designed and performed brain network structural connectivity weight analyses. J.A.G. performed logistic regression analyses. E.R.S. and P.O. wrote the manuscript.

Declaration of Interests

The authors declare no competing interests.

1254 **Extended Data Figure and Figure Legends**

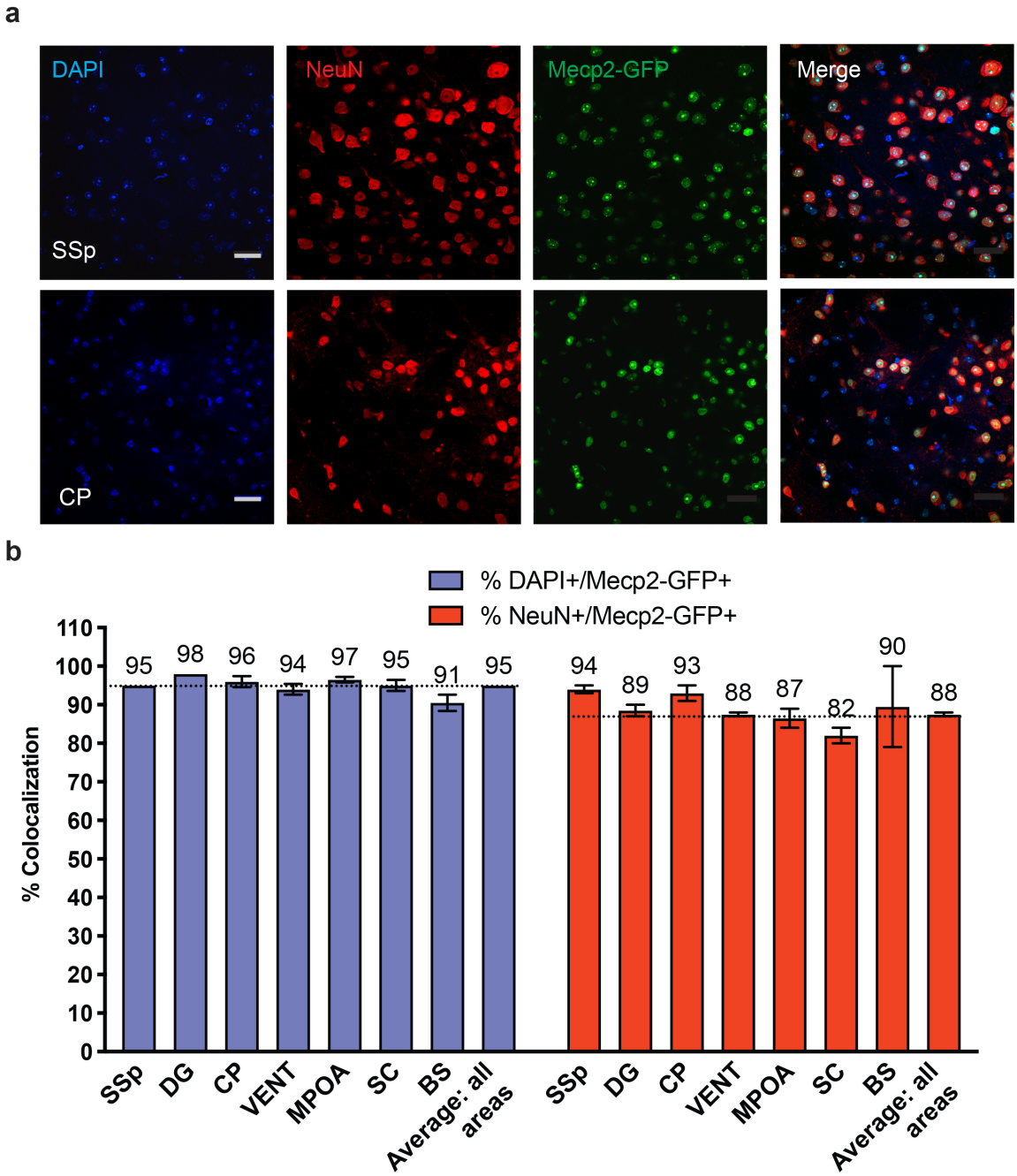

1255

1256 **Extended Data Fig. 1 | Mecp2-GFP allele labels nearly all cells in homozygous Mecp2-**
1257 **GFP(m/p) brain. a**, Representative images of DAPI and NeuN counter-stained sections
1258 from somatosensory cortex (SSp) and caudate putamen (CP) areas in a homozygous
1259 Mecp2-GFP(m/p) brain (scale bar = 25 um). **b**) Quantification of DAPI and NeuN
1260 colocalization with Mecp2-GFP(m/p) expression across seven brain areas (mean ± SD):

1261 SSp = 95 ± 0 and 94 ± 1.41; DG (dentate gyrus) = 98 ± 0 and 89 ± 2.12; CP = 96 ± 1.41
1262 and 93 ± 2.83; VENT (ventral group of the thalamus) = 94 ± 1.41 and 88 ± 0.71; MPOA
1263 (medial preoptic area) = 97 ± 0.71 and 87 ± 3.54; SC (superior colliculus) = 95 ± 1.41 and
1264 82 ± 2.83; BS (brain stem) = 91 ± 2.12 and 90 ± 14.85 from 2 Mecp2-GFP(m/p) brains.
1265 Mean across all areas = 95 ± 0 and 88 ± 0.71.
1266
1267
1268
1269

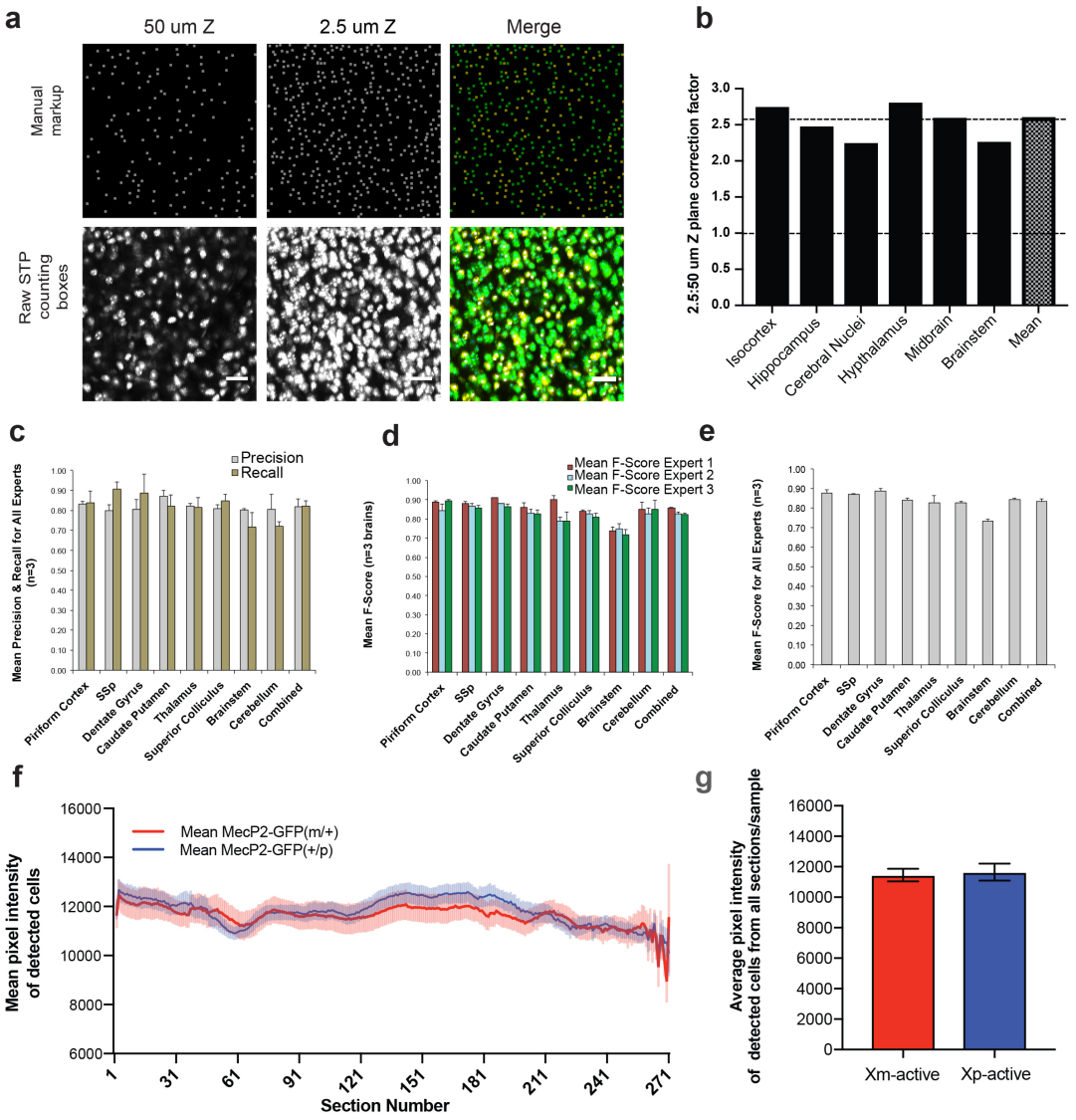

Extended Data Fig. 2 | Validation and benchmarking of Mecp2-GFP+ cell detection. **a**-**b**, Data used to calculate a serial 2D to 3D cell count conversion factor. **a**, An example of a manual cell count markup (top row) and raw STPT image (bottom row) from a homozygous Mecp2-GFP(m/p) brain (ventromedial hypothalamus). Manual markup was made for a 3D brain volume imaged at a Z resolution of 2.5 µm. The 3D manual cell count was compared to a convolutional network (CN) based cell count from a single plane in the middle of the 3D stack. Scale bar = 25 um. **b**) 2D to 3D conversion factors were calculated by dividing the manual 3D cell counts by the single plane CN-based cell count for selected brain areas. The mean conversion factor of 2.6 was then used for all brain regions. **c**-**e**) F-score calculations of CN performance in detecting GFP+ cells based on expert ground truth

1281 data (see Methods). The calculations were performed on 8 select tiles from different brain
1282 regions covering a range of cell densities from 3 Mecp2-GFP(+/p) brain samples. **a**) Mean
1283 CN precision and recall. **b**) Mean CN F-score derived from precision and recall values of
1284 (c) for each individual expert across regions. C) Mean CN F-score shown for all regions.
1285 **f**-**g**) Fluorescence intensity comparisons of Mecp2-GFP+ cell nuclei across genotypes. **f**)
1286 Mean cellular pixel intensity from each section (270 sections total; anterior limit = 1;
1287 posterior limit = 270) of Xm-active (red) or Xp-active (blue) cells. **g**) Group comparison
1288 of mean pixel intensity across all segmented cells. All values = mean ± SEM.
1289
1290
1291
1292
1293
1294
1295
1296
1297
1298
1299
1300
1301
1302
1303
1304
1305
1306
1307
1308
1309
1310

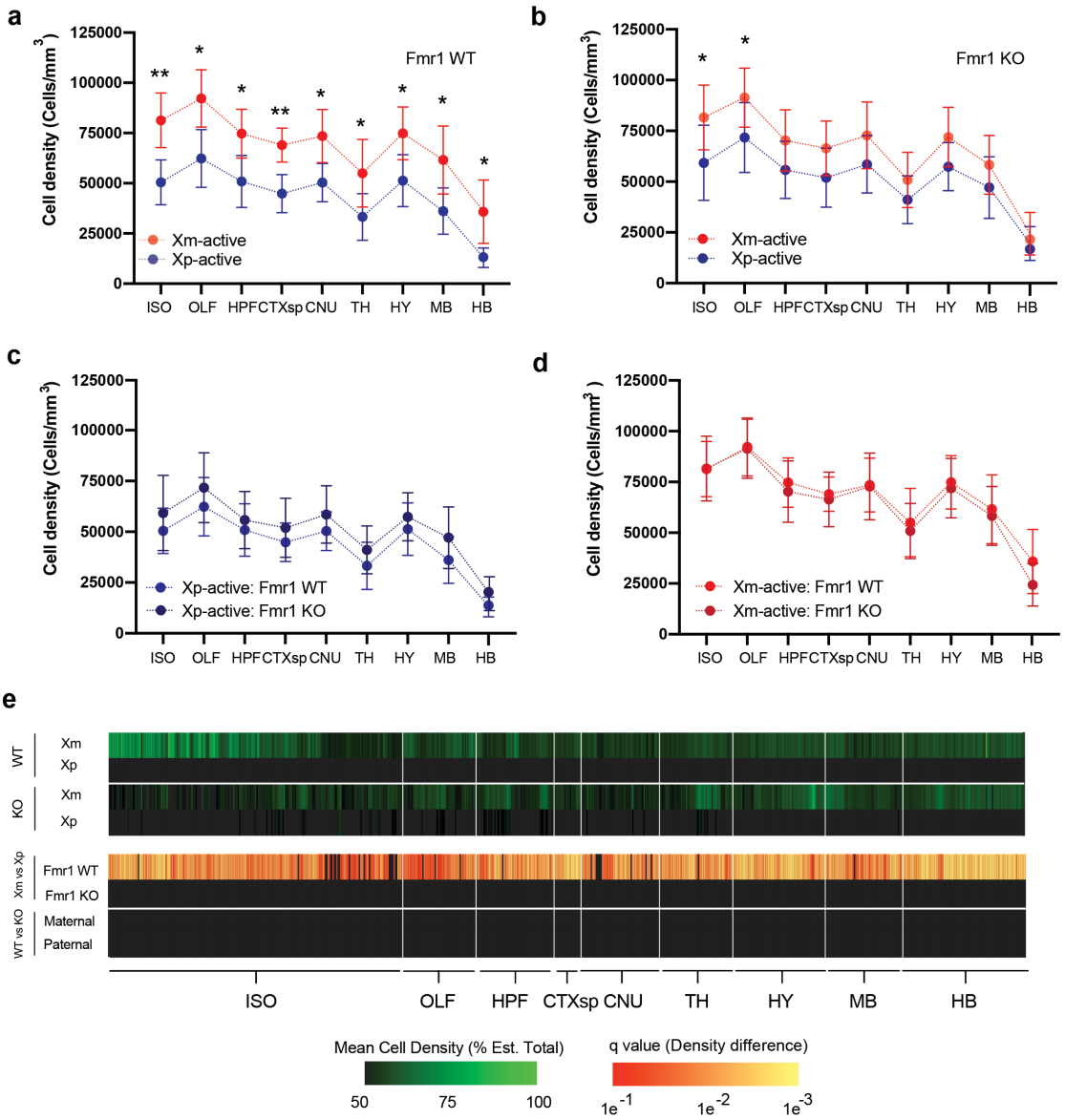

Extended Data Fig. 3 | ROI-based healthy cell density analyses in Fmr1 WT and heterozygous KO mice. a-d, Healthy cell density (cells/mm^3; mean ± SD) comparisons amongst (**a**) Xm-active and Xp-active Fmr1 WT, (**b**) Xm-active and Xp-active Fmr1 KO, (**c**) Xp-active Fmr1 WT and KO, and (**d**) Xm-active Fmr1 WT and KO mice across major ontological divisions of the brain. Fmr1 WT (Xm-active (n=8), Xp-active (n=7): ISO: 81354 ± 13598; 50458 ± 11153; OLF: 92208 ± 14279, 62357 ± 14412; HPF: 74715 ± 12112, 50902 ± 12888; CTXsp: 68989 ± 8458, 44848 ± 9479; CNU: 73486 ± 113216, 50317 ± 9551; TH: 54995 ± 16794, 33252 ± 11610; HY: 74840 ± 13100, 51308 ± 12890; MB: 61564 ± 16908, 36108 ±11524; HB: 35855 ± 15759 versus 12918 ± 4819) or

1321 heterozygous KO mice (Xm-active (n=7), Xp-active (n=8): ISO: 83006 ± 15294, 54469 ±
1322 13584; OLF: 92689 ± 13965, 67429 ± 13076; HPF: 71677 ± 14524, 52120 ± 10280;
1323 CTXsp: 67988 ± 13240, 48068 ± 10198; CNU: 74039 ± 15614, 55089 ± 10992; TH: 51358
1324 ± 12678, 39105 ± 11187; HY: 72572 ± 13680, 54570 ± 9459; MB: 60011 ± 14278, 43524
1325 ± 12182; HB: 25308 ± 10080, 17737 ± 7177) *p<0.05, **p<0.01, 2-way mixed effects
1326 ANOVA with Holm-Sidak multiple comparison correction. **e**) Brain-wide cell density
1327 comparisons in Fmr1 WT and heterozygous KO mice. Columns 1-4: Brain-wide heat map
1328 visualization of mean healthy Xm-active and Xp-active ROI cell densities (% of estimated
1329 total) on a color gradient of black (50%) to green (100%) amongst Fmr1 WT and KO mice.
1330 Columns 5-8: Brain-wide q values of ROI cell density statistical comparisons of active XC
1331 parent-of-origin amongst Fmr1 WT and Fmr1 KO mice (top), and cell density comparisons
1332 amongst mice with WT or KO Fmr1 alleles with matched active XC parent-of-origin
1333 (bottom). Legends indicating color scaling for mean cell density (left) and q values (right)
1334 are listed at the bottom.
1335

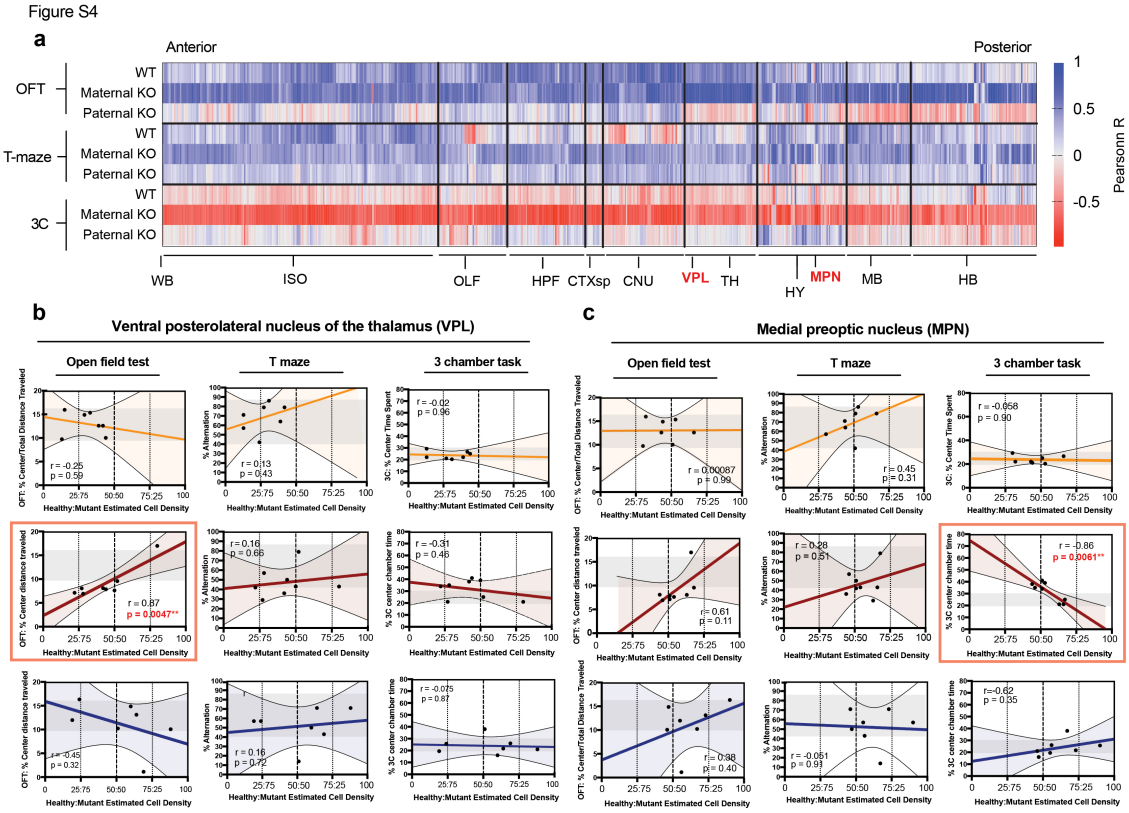

Extended Data Fig. 4 | Identification of two sets of brain regions with local Fmr1-WT:KO cell ratios linked to phenotypes in the OFT and 3-chamber test: Raw Pearson r values and scatterplot examples across genetic groups and behavioral tests. a, 2D heat maps of raw Pearson correlation r values corresponding to **Fig 4a** across brain ROIs grouped by major ontological structures from anterior (left) to posterior (right) positions of the whole-brain. Raw Pearson r values are represented on a color gradient scale from -1 (red) to 0 (white) to 1 (blue). Results from Fmr1 WT ("WT"), maternal Fmr1-KO(m)/Mecp2-GFP(p) ("Maternal KO") and paternal Fmr1-KO(p)/Mecp2-GFP(m) ("Paternal KO") mice are grouped by each behavioral test: top: OFT, middle: T maze, bottom: 3-chamber (3C). **b**-**c**, Individual scatterplot visualization of the data from (**a**) for each behavioral group and behavioral test for the (**b**) ventral posterolateral nucleus of the thalamus (VPL), and (**c**) medial preoptic nucleus (MPN). Raw r and p values of statistical tests are inlayed within each panel. Red boxes bound correlations that reached statistical significance.

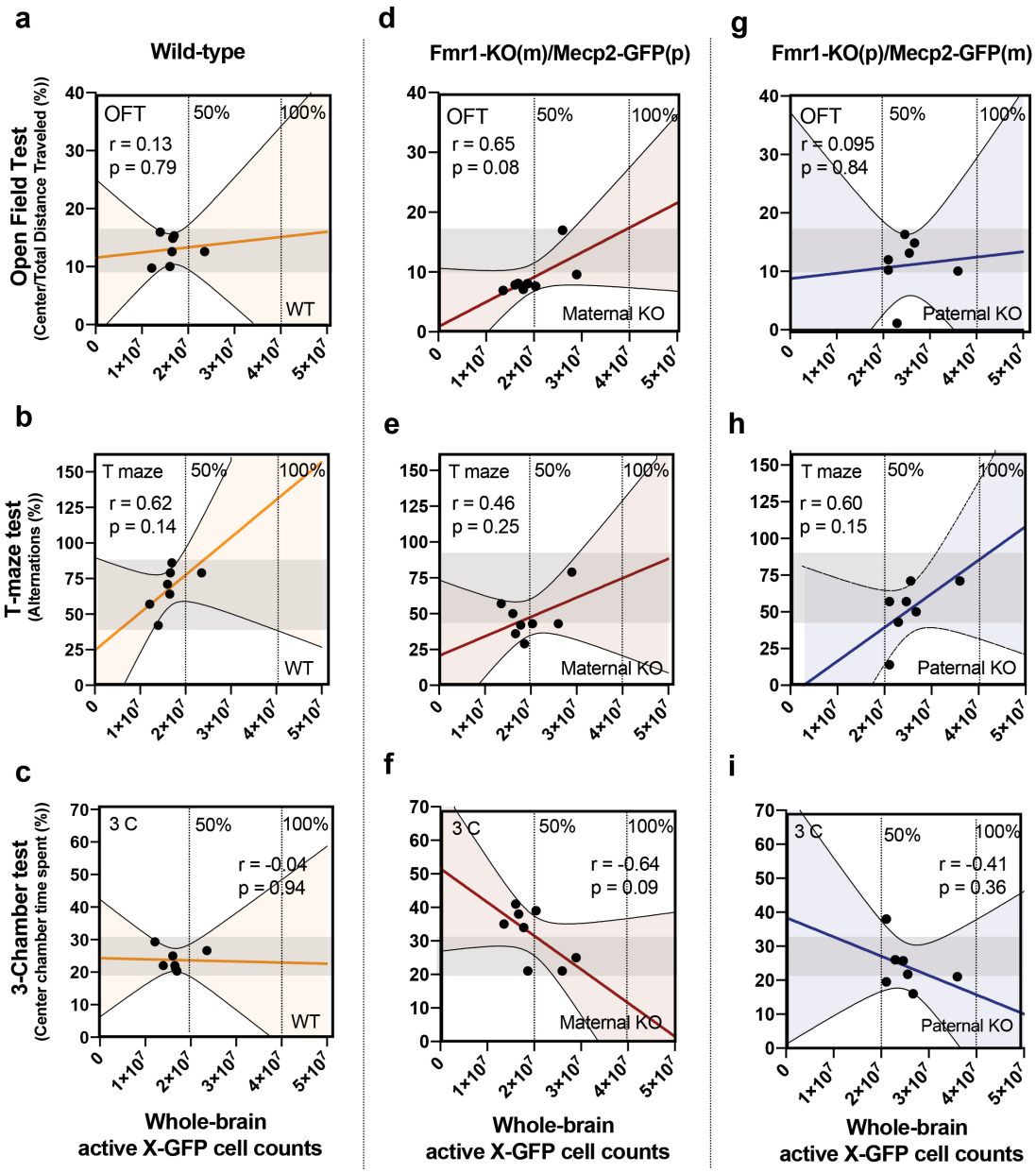

Extended Data Fig. 5 | Whole-brain cell count correlations with behavior. (**a**-**c**; left) Fmr1 WT, (**d**-**f**; center) maternal Fmr1 KO, and (**g**-**i**; right) paternal Fmr1 KO whole-brain cell counts correlated to (**a**, **d**, **g**; top) OFT, (**b**, **e**, **h**; middle) T maze, and (**c**, **f**, **i**; bottom) 3 chamber behavioral scores. Dashed lines indicate estimated 50 and 100% cell counts. Gray transparent boxes inside plots indicate Fmr1 WT range of behavioral scores for comparison across mutant groups. r and p value statistics are listed in each panel.

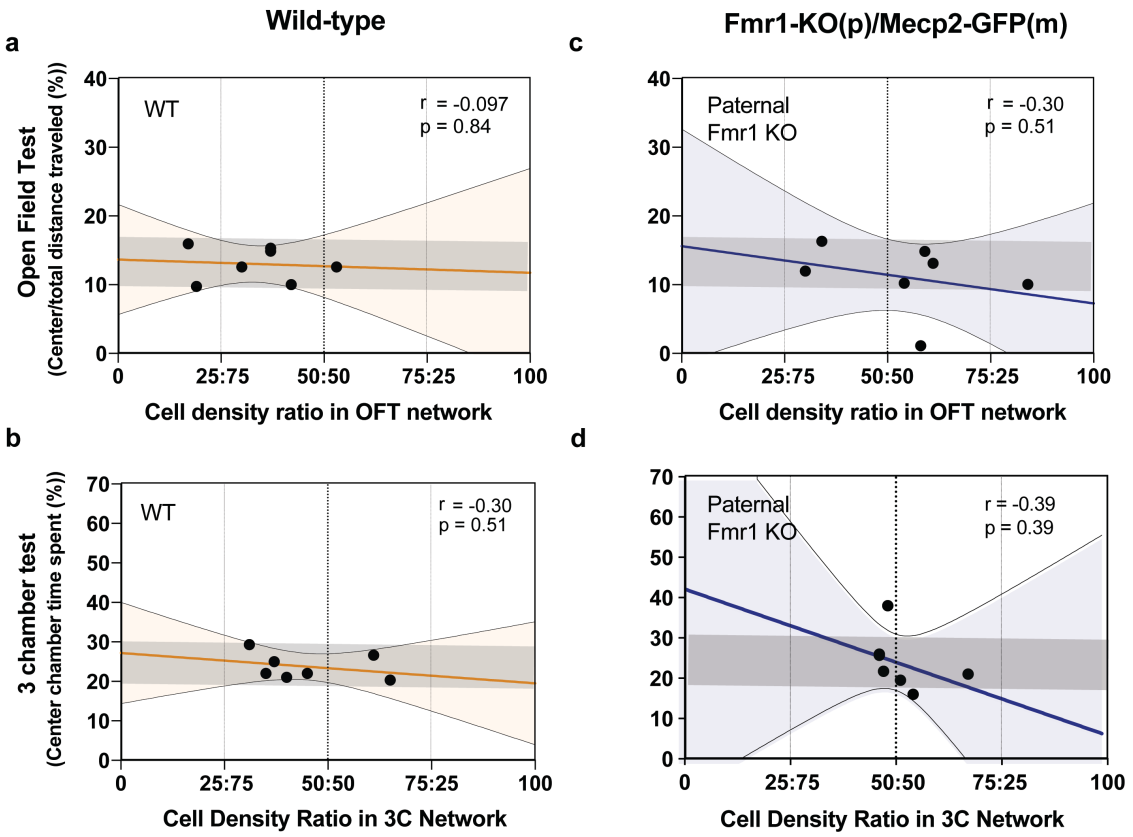

Extended Data Fig. 6 | Control group correlations of behavioral brain network cell density ratios with behavioral scores. Fmr1 WT (**a**, **b**; left) and paternal Fmr1 KO (**c**, **d**; right) linear regression models of ROI network cell density ratios and scores from (**a**, **c**; top) OFT and (**b**, **d**; bottom) 3C behavioral assays. Regression and statistical test values are listed for each panel.

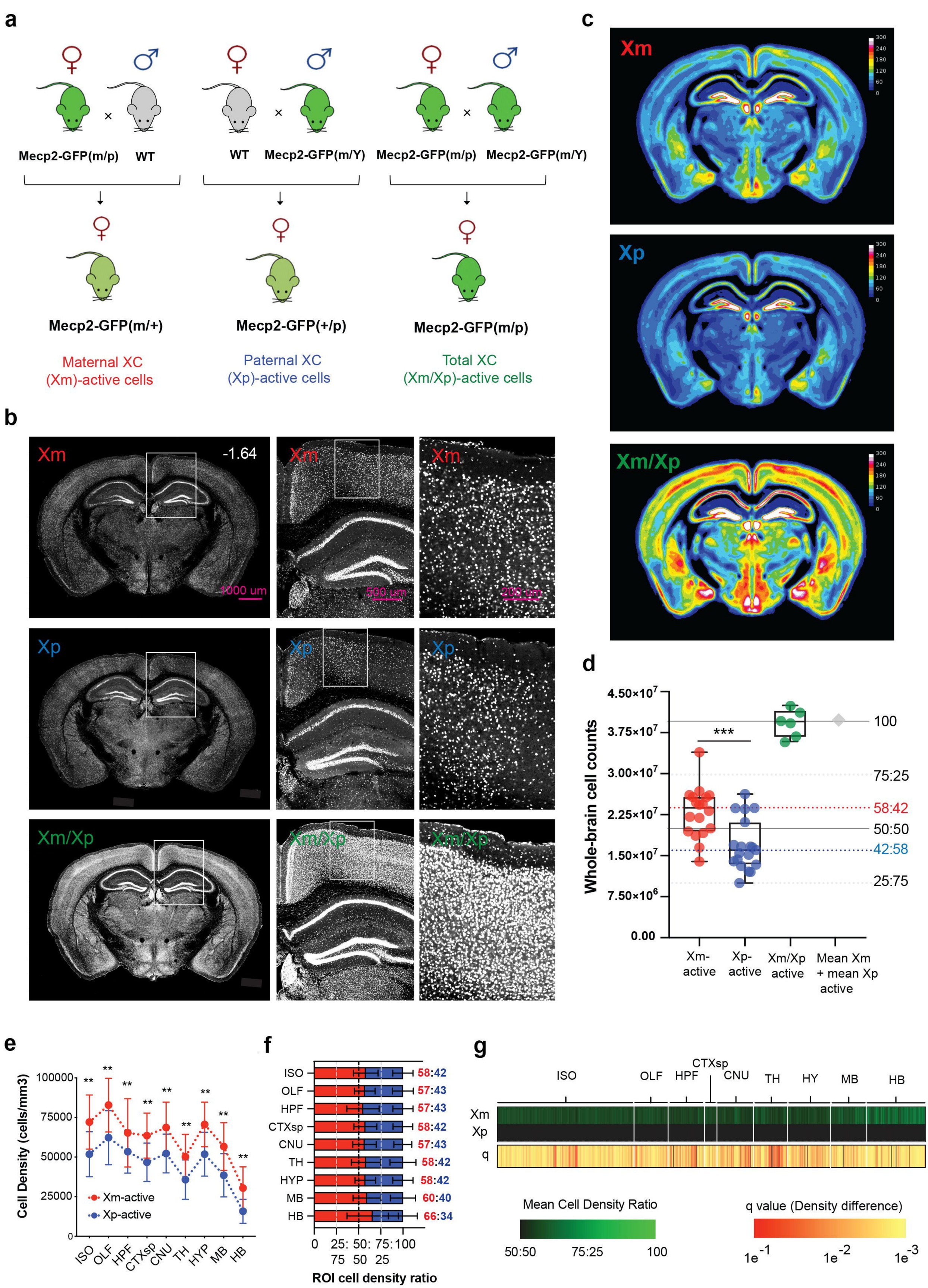
a
Mecp2-GFP(m/p)
WT
WT
Mecp2-GFP(m/Y)
Mecp2-GFP(m/p)
Mecp2-GFP(m/Y)
Mecp2-GFP(m/+)
Maternal XC
(Xm)-active cells
Mecp2-GFP(+/p)
Paternal XC
(Xp)-active cells
Mecp2-GFP(m/p)
Total XC
(Xm/Xp)-active cells
b
Xm
-1.64
1000 um
500 um
200 um
Xp
Xm/Xp
c
Xm
Xp
Xm/Xp
d
Whole-brain cell counts
4.50×10^7
3.75×10^7
3.00×10^7
2.25×10^7
1.50×10^7
7.50×10^6
0.00
***
100
75:25
58:42
50:50
42:58
25:75
Xm-active
Xp-active
Xm/Xp active
Mean Xm + mean Xp active
e
Cell Density (cells/mm3)
100000
75000
50000
25000
0
Xm-active
Xp-active
ISO
OLF
HPF
CTXsp
CNU
TH
HYP
MB
HB
f
ISO 58:42
OLF 57:43
HPF 57:43
CTXsp 58:42
CNU 57:43
TH 58:42
HYP 58:42
MB 60:40
HB 66:34
0 25:75 50:50 75:25 100
ROI cell density ratio
g
ISO
OLF
HPF
CTXsp
CNU
TH
HY
MB
HB
Xm
Xp
q
Mean Cell Density Ratio
50:50
75:25
100
q value (Density difference)
1e^-1
1e^-2
1e^-3

a

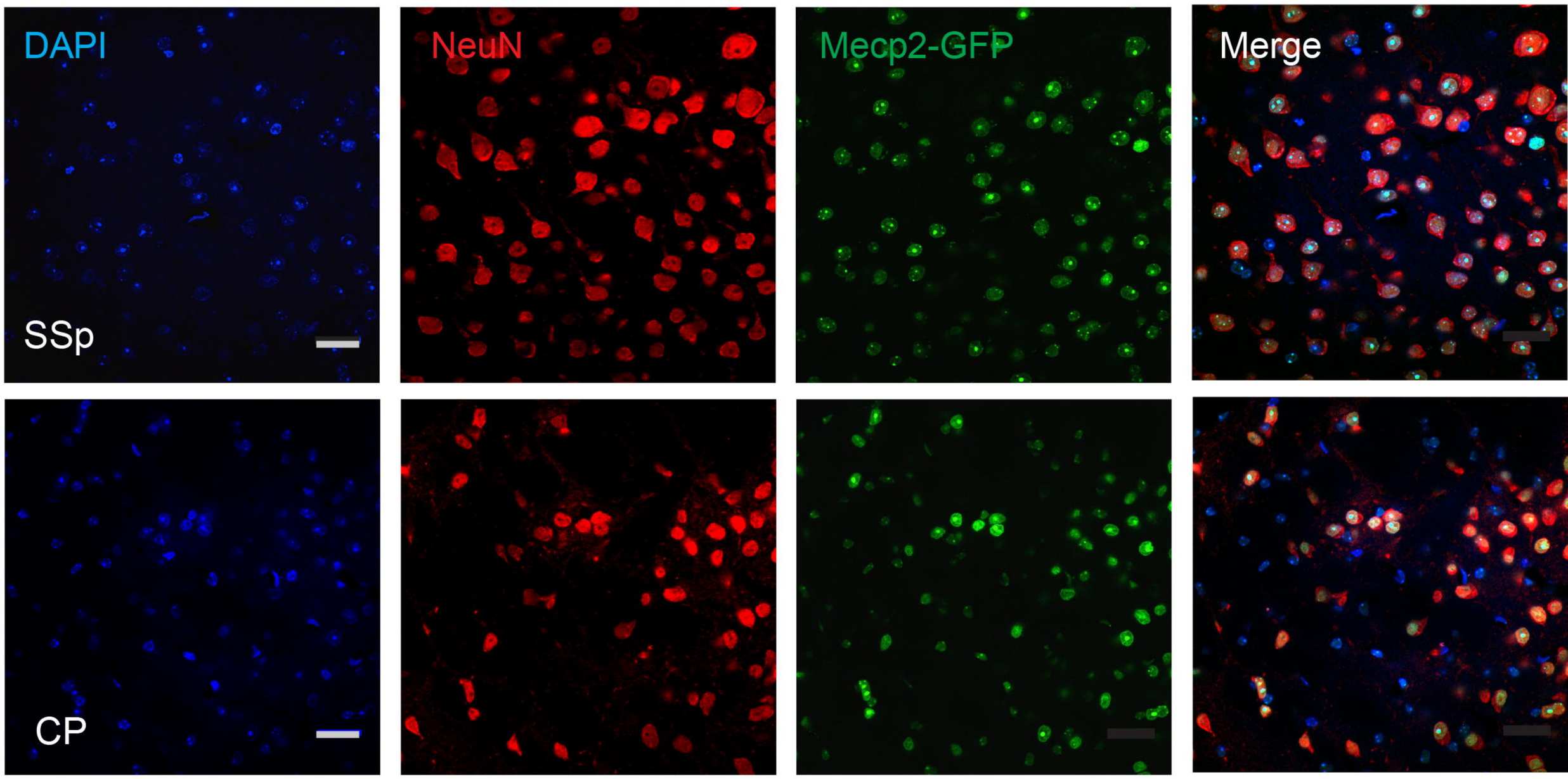
DAPI
NeuN
Mecp2-GFP
Merge
SSp
CP

b

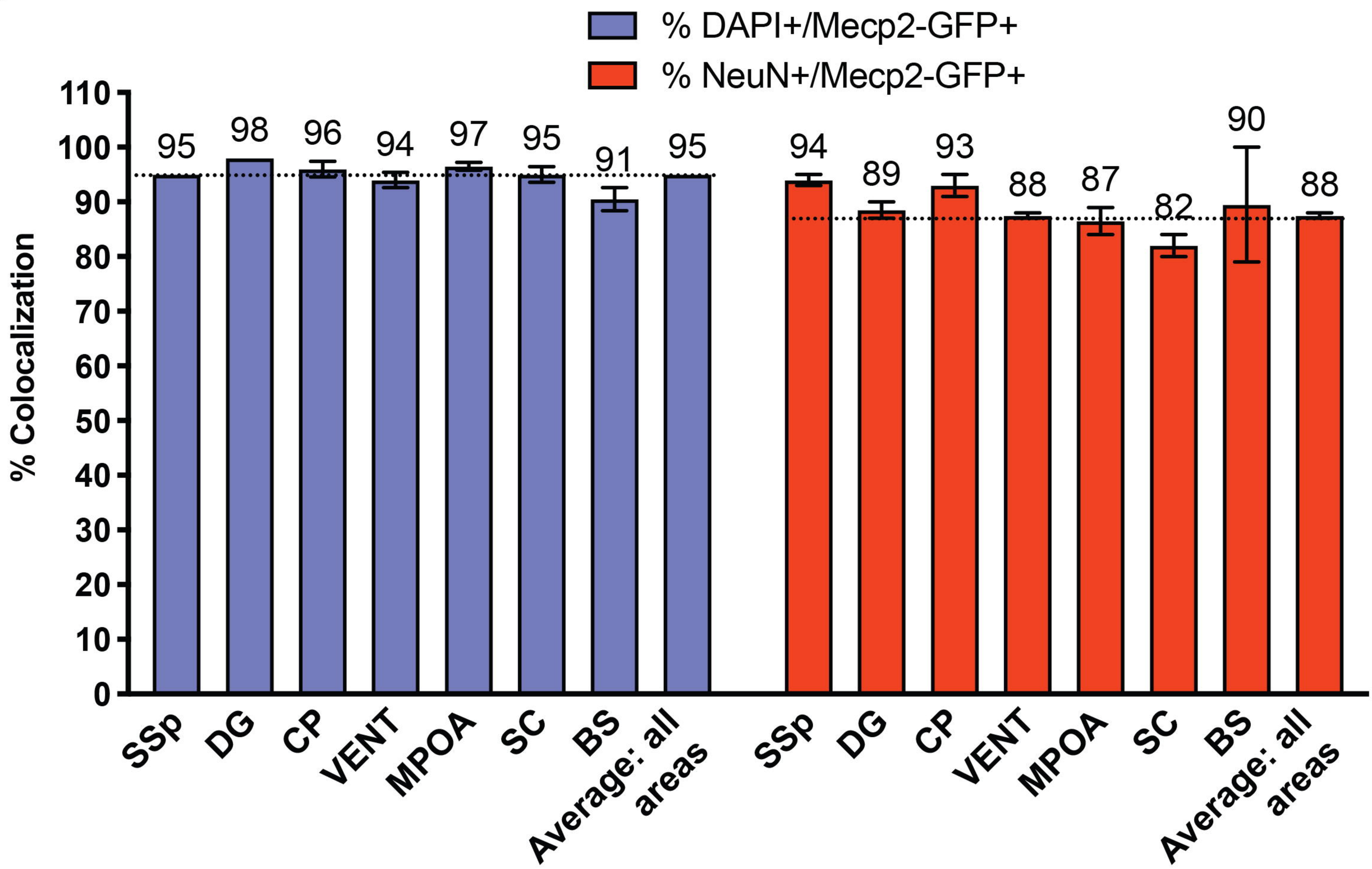
% DAPI+/Mecp2-GFP+
% NeuN+/Mecp2-GFP+
% Colocalization
110
100
90
80
70
60
50
40
30
20
10
0
95
98
96
94
97
95
91
95
94
89
93
88
87
82
90
88
SSp
DG
CP
VENT
MPOA
SC
BS
Average: all areas
SSp
DG
CP
VENT
MPOA
SC
BS
Average: all areas

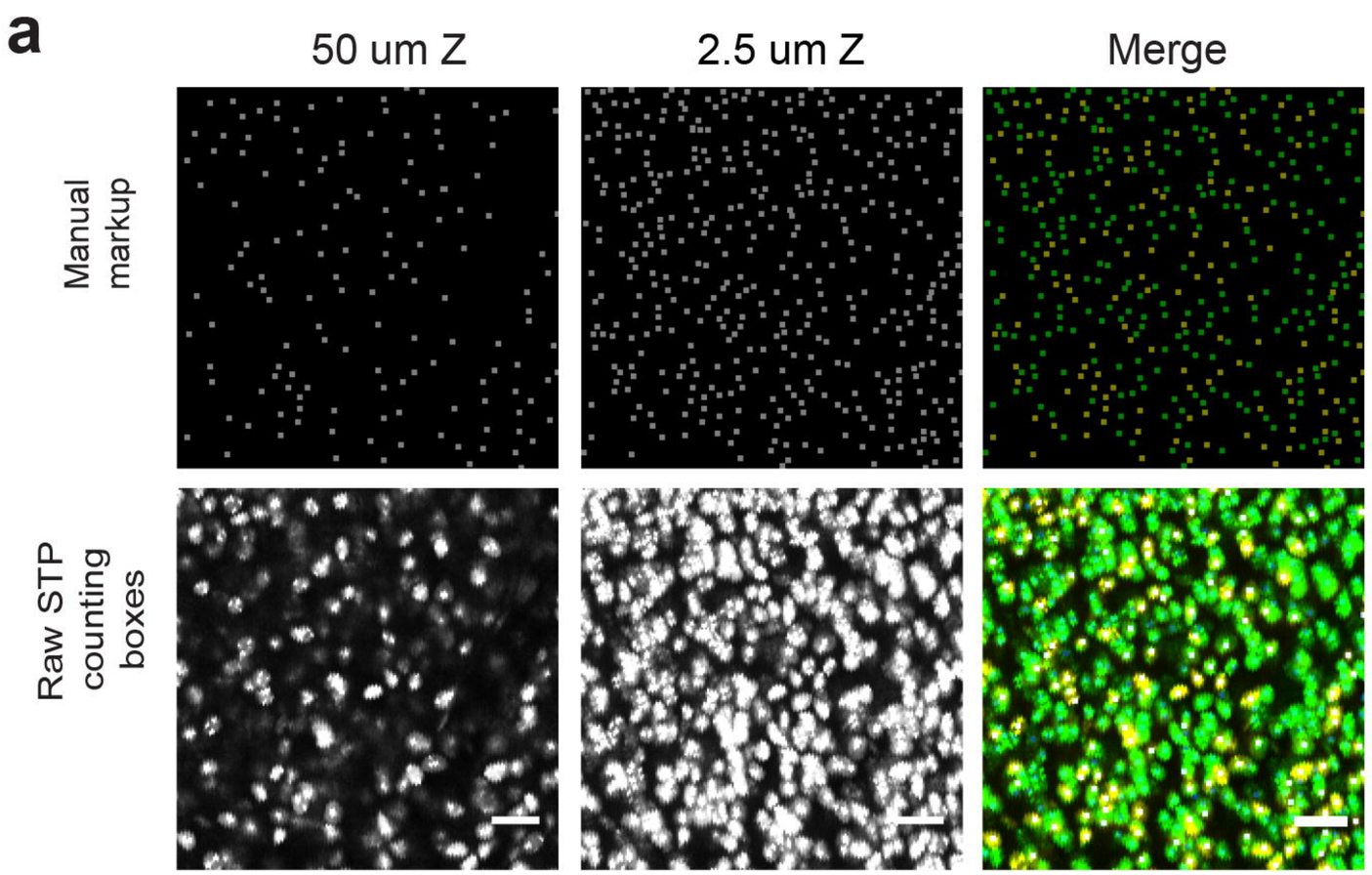
a
50 um Z
2.5 um Z
Merge
Manual markup
Raw STP counting boxes

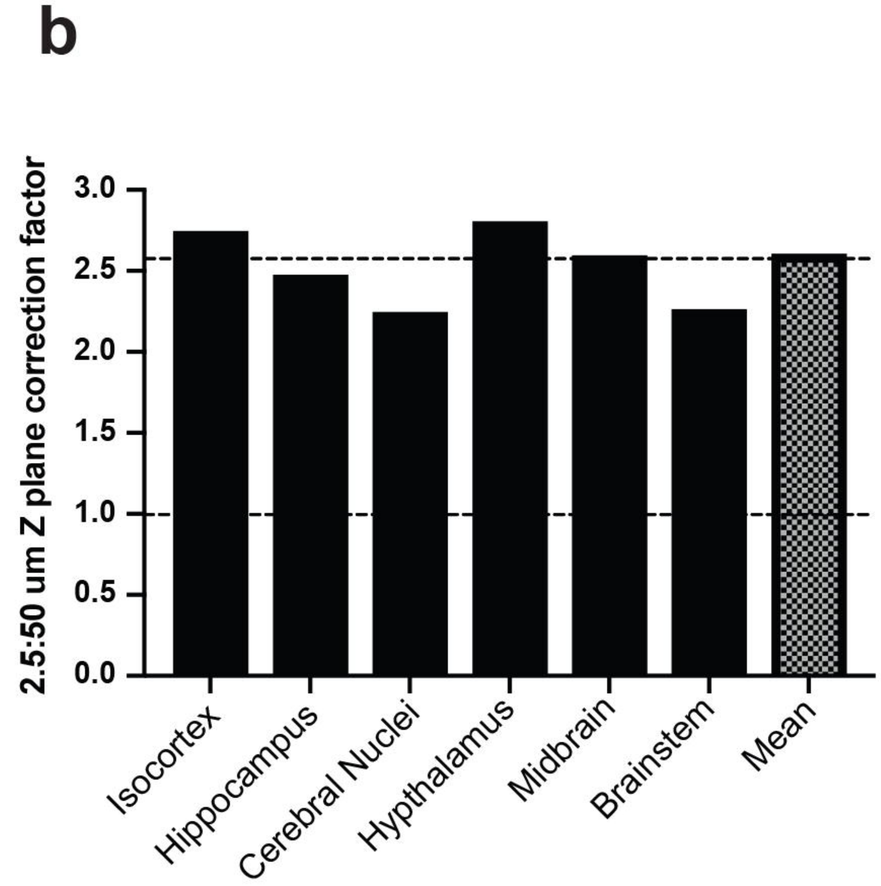
b
2.5:50 um Z plane correction factor
3.0
2.5
2.0
1.5
1.0
0.5
0.0
Isocortex
Hippocampus
Cerebral Nuclei
Hypthalamus
Midbrain
Brainstem
Mean

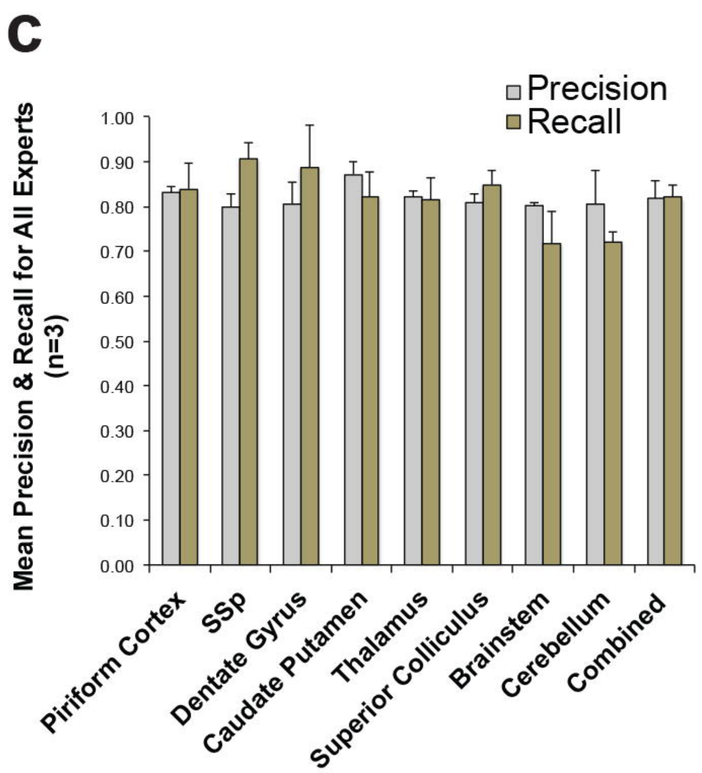
c
Precision
Recall
Mean Precision & Recall for All Experts (n=3)
1.00
0.90
0.80
0.70
0.60
0.50
0.40
0.30
0.20
0.10
0.00
Piriform Cortex
SSp
Dentate Gyrus
Caudate Putamen
Thalamus
Superior Colliculus
Brainstem
Cerebellum
Combined

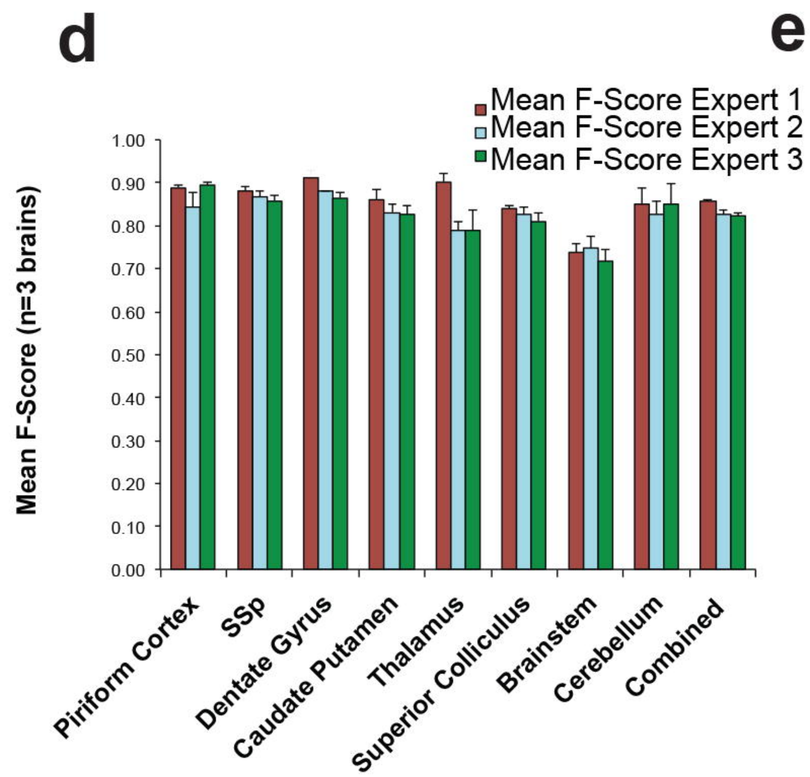
d
Mean F-Score Expert 1
Mean F-Score Expert 2
Mean F-Score Expert 3
Mean F-Score (n=3 brains)
1.00
0.90
0.80
0.70
0.60
0.50
0.40
0.30
0.20
0.10
0.00
Piriform Cortex
SSp
Dentate Gyrus
Caudate Putamen
Thalamus
Superior Colliculus
Brainstem
Cerebellum
Combined

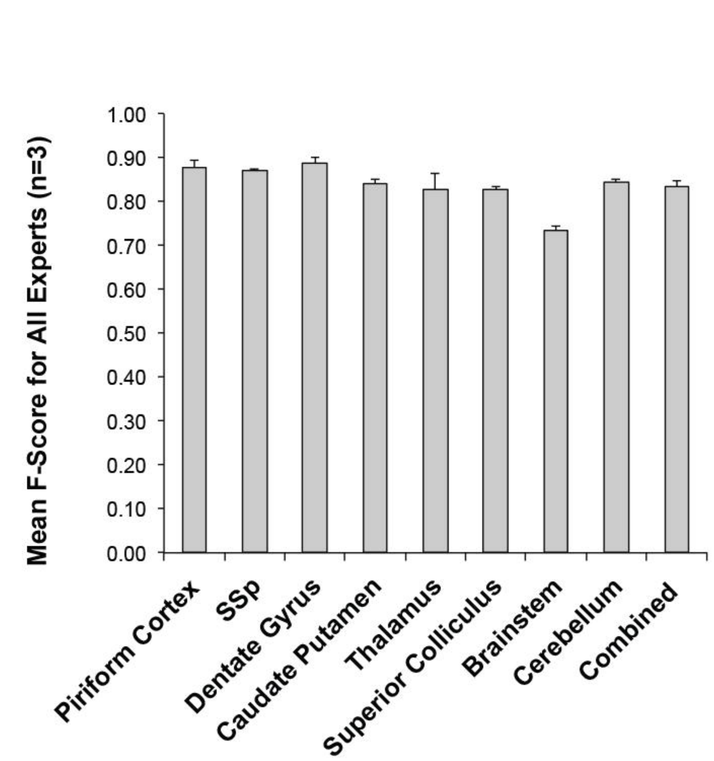
e
Mean F-Score for All Experts (n=3)
1.00
0.90
0.80
0.70
0.60
0.50
0.40
0.30
0.20
0.10
0.00
Piriform Cortex
SSp
Dentate Gyrus
Caudate Putamen
Thalamus
Superior Colliculus
Brainstem
Cerebellum
Combined

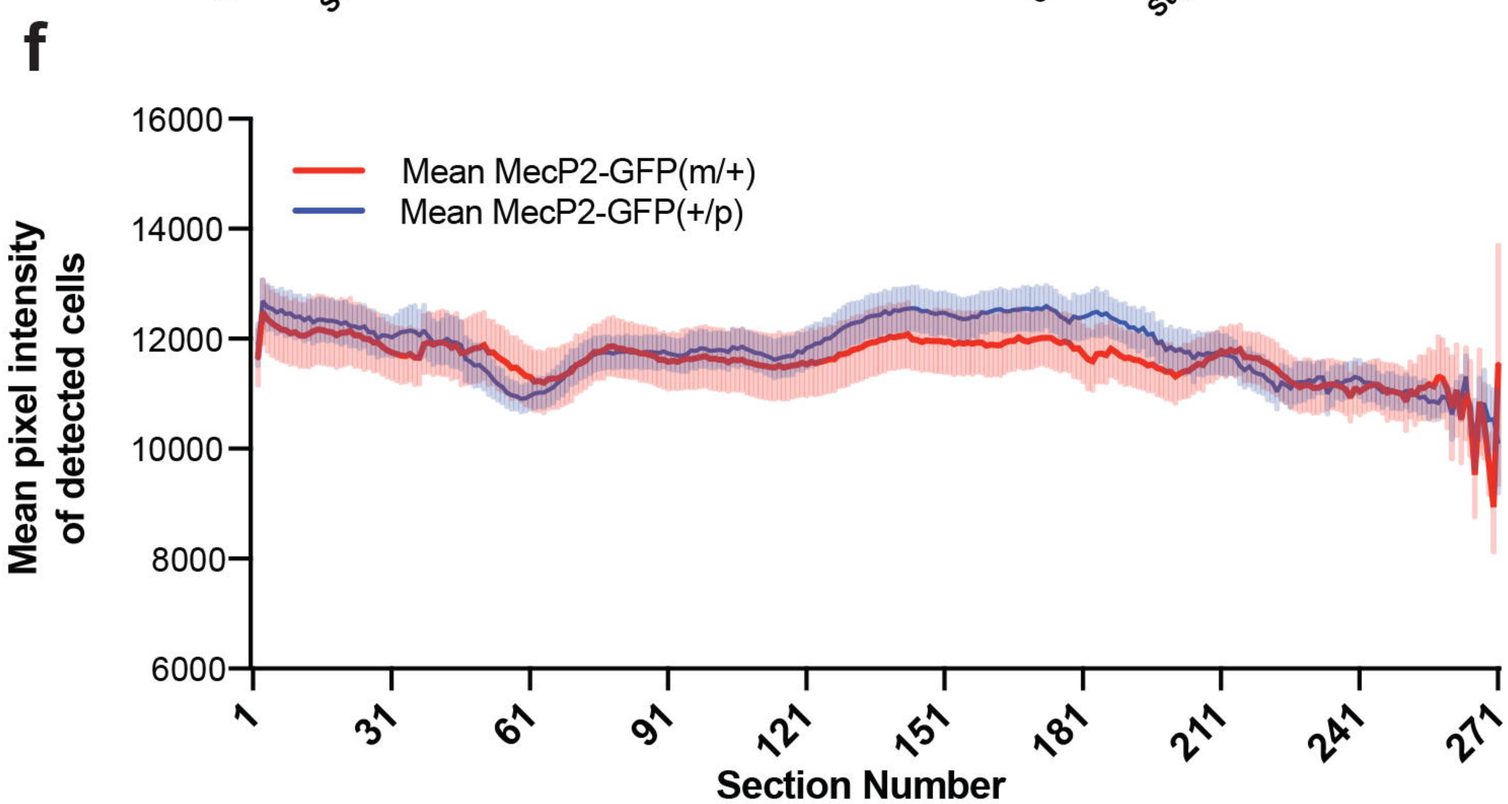
f
Mean MecP2-GFP(m/+)
Mean MecP2-GFP(+/p)
Mean pixel intensity of detected cells
16000
14000
12000
10000
8000
6000
1
31
61
91
121
151
181
211
241
271
Section Number

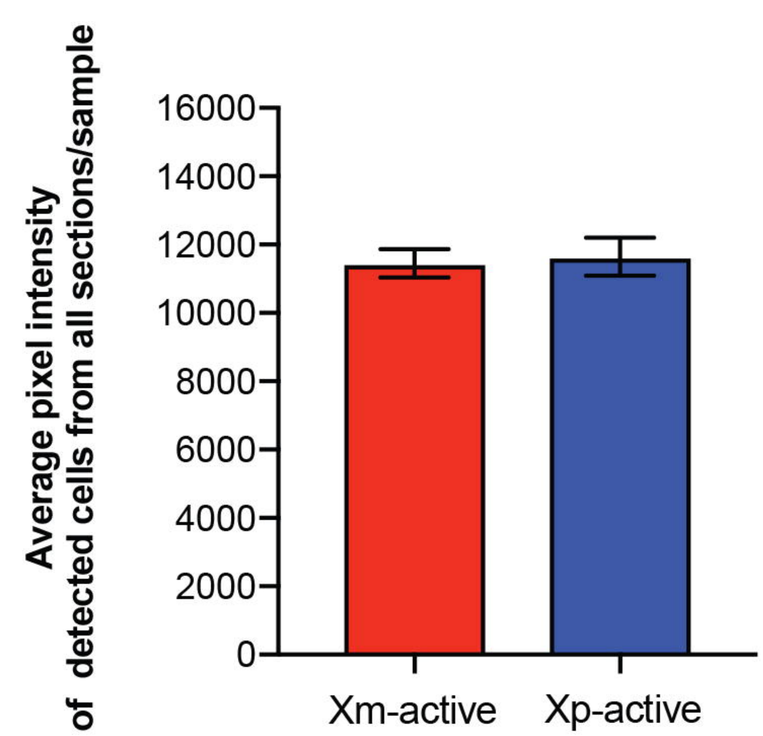
g
Average pixel intensity of detected cells from all sections/sample
16000
14000
12000
10000
8000
6000
4000
2000
0
Xm-active
Xp-active

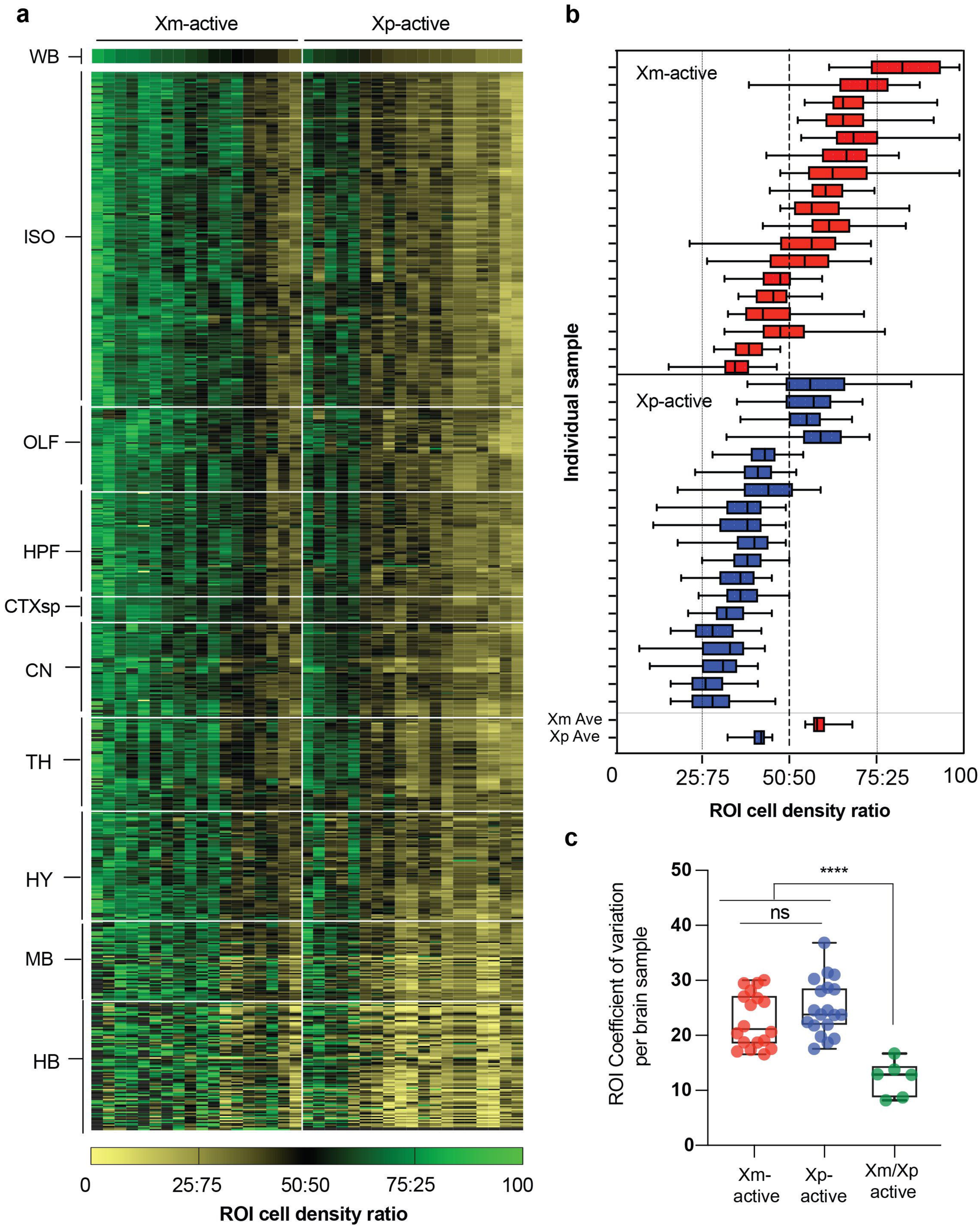
a
Xm-active
Xp-active
WB
ISO
OLF
HPF
CTXsp
CN
TH
HY
MB
HB
0
25:75
50:50
75:25
100
ROI cell density ratio
b
Xm-active
Xp-active
Individual sample
Xm Ave
Xp Ave
0
25:75
50:50
75:25
100
ROI cell density ratio
c
ROI Coefficient of variation per brain sample
50
40
30
20
10
0
****
ns
Xm-active
Xp-active
Xm/Xp active

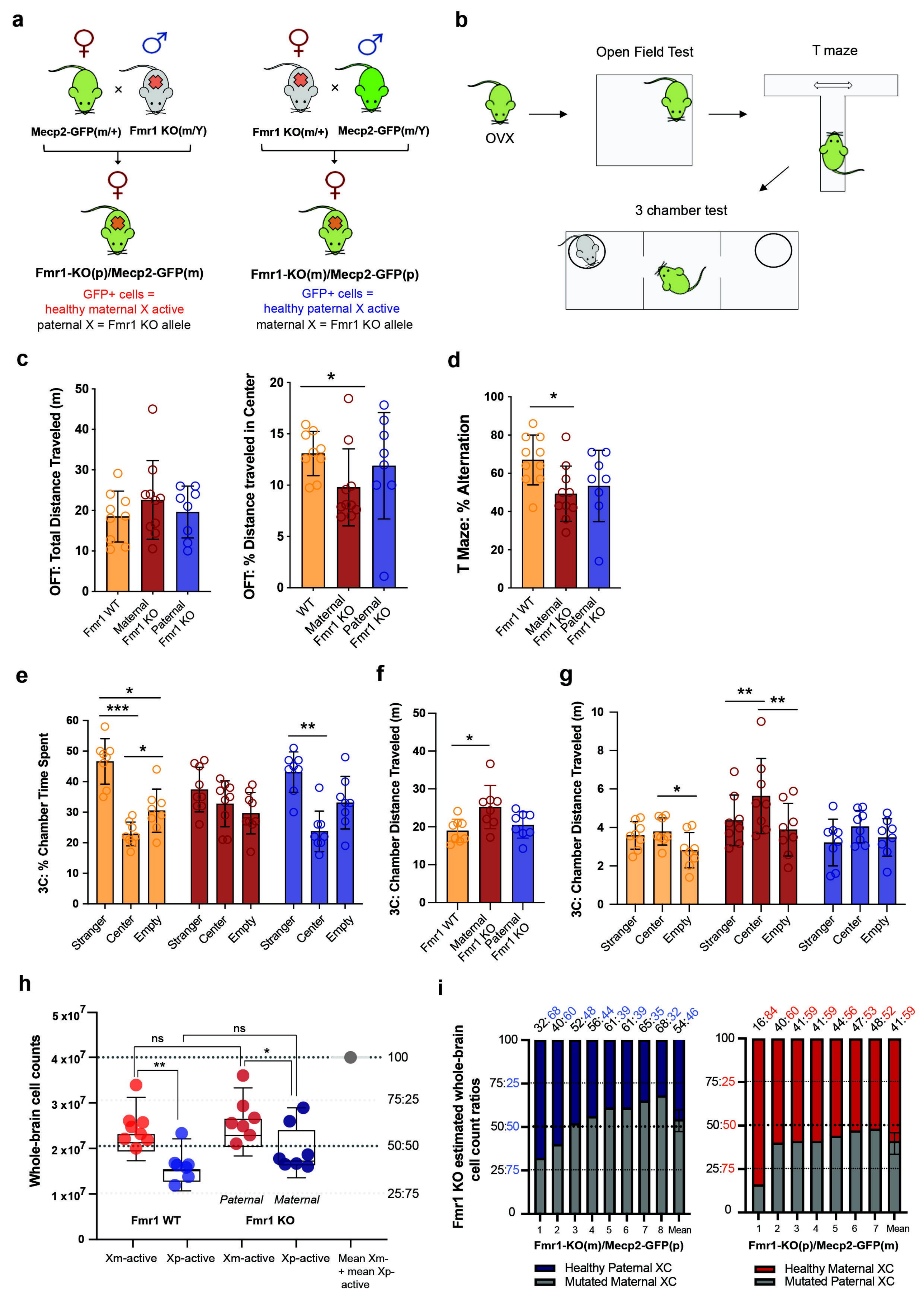
a
Mecp2-GFP(m/+)
Fmr1 KO(m/Y)
Fmr1-KO(p)/Mecp2-GFP(m)
GFP+ cells =
healthy maternal X active
paternal X = Fmr1 KO allele
Fmr1 KO(m/+)
Mecp2-GFP(m/Y)
Fmr1-KO(m)/Mecp2-GFP(p)
GFP+ cells =
healthy paternal X active
maternal X = Fmr1 KO allele
b
OVX
Open Field Test
T maze
3 chamber test
c
OFT: Total Distance Traveled (m)
OFT: % Distance traveled in Center
Fmr1 WT
Maternal Fmr1 KO
Paternal Fmr1 KO
d
T Maze: % Alternation
e
3C: % Chamber Time Spent
Stranger
Center
Empty
f
3C: Chamber Distance Traveled (m)
g
3C: Chamber Distance Traveled (m)
h
Whole-brain cell counts
ns
Paternal
Maternal
Fmr1 WT
Fmr1 KO
Xm-active
Xp-active
Mean Xm- + mean Xp-active
i
Fmr1 KO estimated whole-brain cell count ratios
Fmr1-KO(m)/Mecp2-GFP(p)
Fmr1-KO(p)/Mecp2-GFP(m)
Healthy Paternal XC
Mutated Maternal XC
Healthy Maternal XC
Mutated Paternal XC

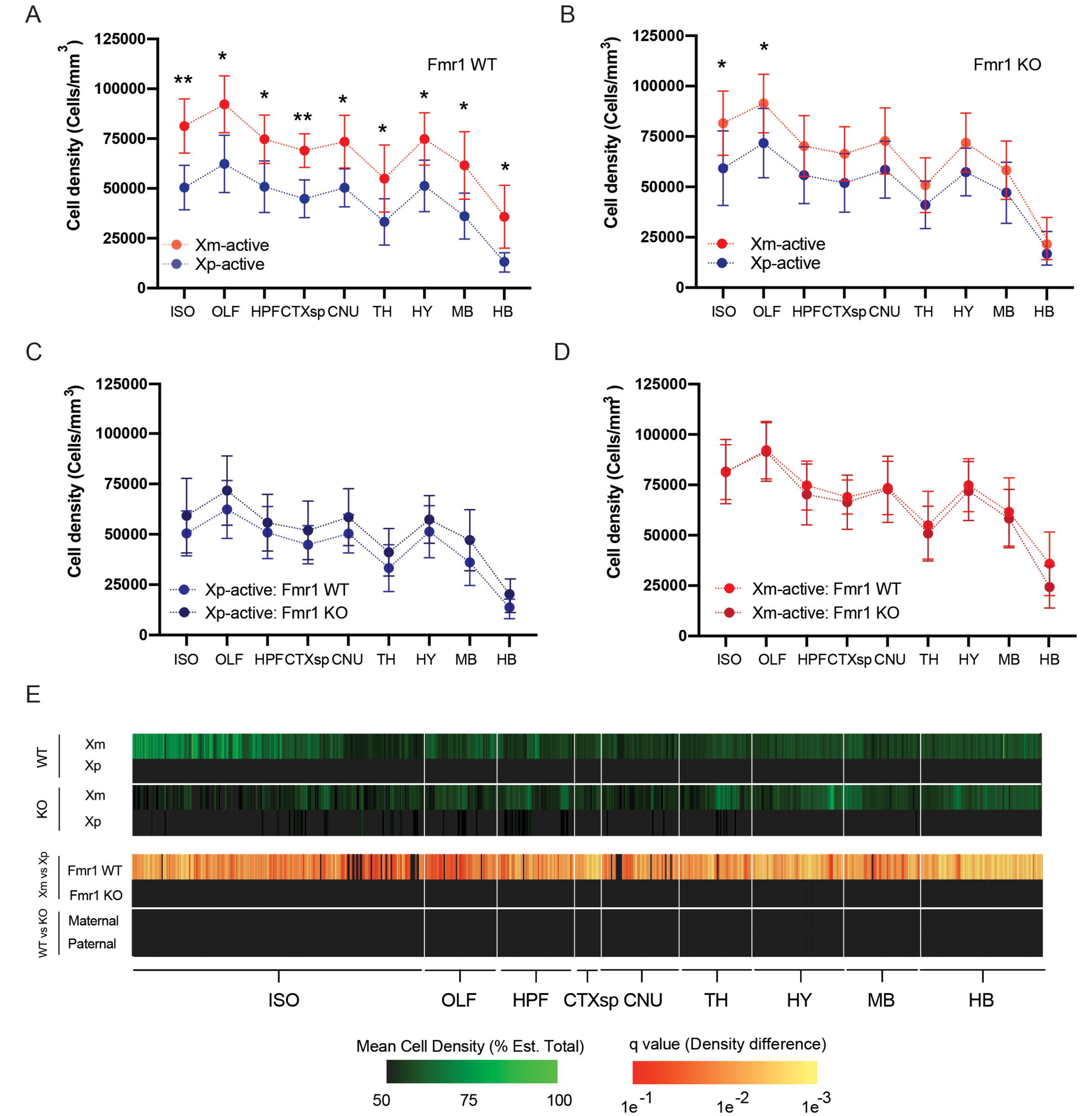
A
Fmr1 WT
Cell density (Cells/mm3)
125000
100000
75000
50000
25000
0
Xm-active
Xp-active
ISO OLF HPF CTXsp CNU TH HY MB HB
B
Fmr1 KO
Cell density (Cells/mm3)
Xm-active
Xp-active
ISO OLF HPF CTXsp CNU TH HY MB HB
C
Cell density (Cells/mm3)
Xp-active: Fmr1 WT
Xp-active: Fmr1 KO
ISO OLF HPF CTXsp CNU TH HY MB HB
D
Cell density (Cells/mm3)
Xm-active: Fmr1 WT
Xm-active: Fmr1 KO
ISO OLF HPF CTXsp CNU TH HY MB HB
E
WT
Xm
Xp
KO
Xm
Xp
Xm vs Xp
Fmr1 WT
Fmr1 KO
WT vs KO
Maternal
Paternal
ISO OLF HPF CTXsp CNU TH HY MB HB
Mean Cell Density (% Est. Total)
50 75 100
q value (Density difference)
1e-1 1e-2 1e-3

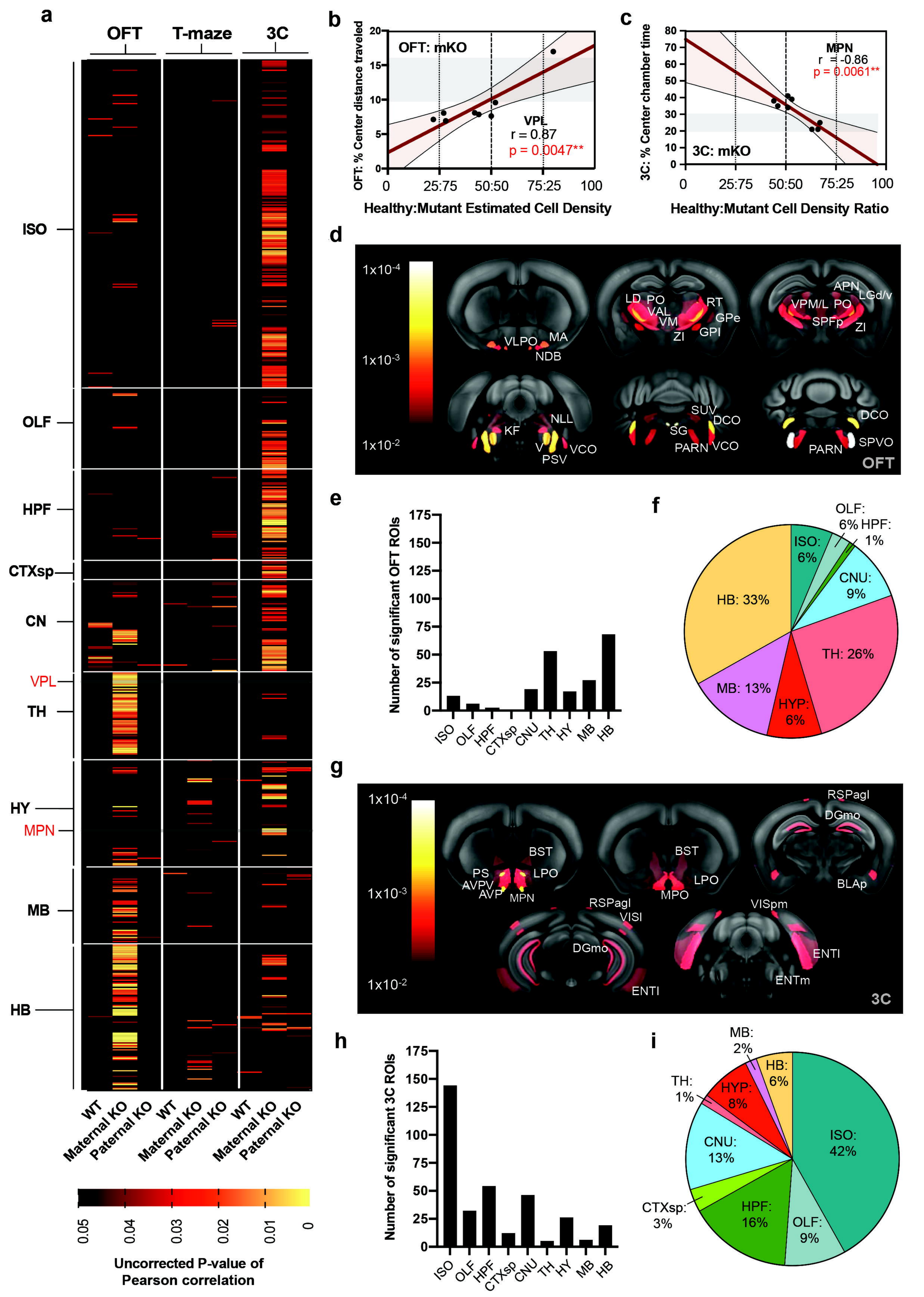
a
OFT
T-maze
3C
ISO
OLF
HPF
CTXsp
CN
VPL
TH
HY
MPN
MB
HB
WT
Maternal KO
Paternal KO
0.05
0.04
0.03
0.02
0.01
0
Uncorrected P-value of Pearson correlation
b
OFT: mKO
VPL
r = 0.87
p = 0.0047**
OFT: % Center distance traveled
Healthy:Mutant Estimated Cell Density
c
MPN
r = -0.86
p = 0.0061**
3C: mKO
3C: % Center chamber time
Healthy:Mutant Cell Density Ratio
d
1x10-4
1x10-3
1x10-2
VLPO
MA
NDB
LD
PO
VAL
VM
RT
GPe
ZI
GPI
APN
LGd/v
VPM/L
PO
SPFp
ZI
KF
NLL
V
VCO
PSV
SUV
DCO
SG
PARN
VCO
DCO
PARN
SPVO
OFT
e
Number of significant OFT ROIs
ISO
OLF
HPF
CTXsp
CNU
TH
HY
MB
HB
f
ISO: 6%
OLF: 6%
HPF: 1%
CNU: 9%
TH: 26%
HYP: 6%
MB: 13%
HB: 33%
g
1x10-4
1x10-3
1x10-2
BST
PS
LPO
AVPV
AVP
MPN
BST
LPO
MPO
RSPagl
VISl
DGmo
ENTl
RSPagl
DGmo
BLAp
VISpm
ENTl
ENTm
3C
h
Number of significant 3C ROIs
ISO
OLF
HPF
CTXsp
CNU
TH
HY
MB
HB
i
MB: 2%
HB: 6%
TH: 1%
HYP: 8%
CNU: 13%
ISO: 42%
CTXsp: 3%
HPF: 16%
OLF: 9%

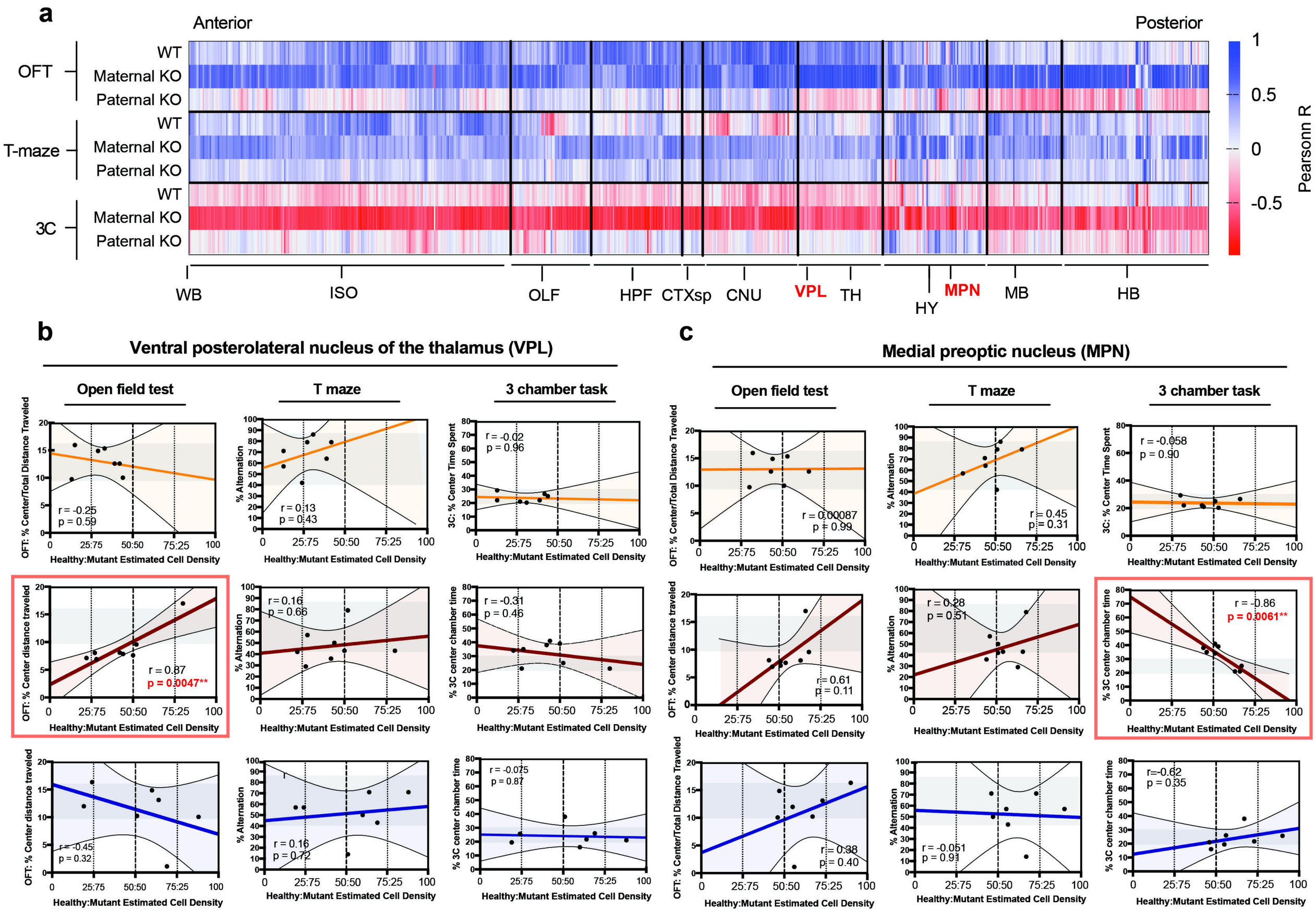
a
Anterior
Posterior
OFT
T-maze
3C
WT
Maternal KO
Paternal KO
Pearsonn R
1
0.5
0
-0.5
WB
ISO
OLF
HPF
CTXsp
CNU
VPL
TH
HY
MPN
MB
HB
b
Ventral posterolateral nucleus of the thalamus (VPL)
Open field test
T maze
3 chamber task
OFT: % Center/Total Distance Traveled
% Alternation
3C: % Center Time Spent
OFT: % Center distance traveled
% 3C center chamber time
Healthy:Mutant Estimated Cell Density
r = -0.25
p = 0.59
r = 0.13
p = 0.43
r = -0.02
p = 0.96
r = 0.87
p = 0.0047**
r = 0.16
p = 0.66
r = -0.31
p = 0.46
r = -0.45
p = 0.32
r = 0.16
p = 0.72
r = -0.075
p = 0.87
c
Medial preoptic nucleus (MPN)
r = 0.00087
p = 0.99
r = 0.45
p = 0.31
r = -0.058
p = 0.90
r = 0.61
p = 0.11
r = 0.28
p = 0.51
r = -0.86
p = 0.0061**
r = 0.38
p = 0.40
r = -0.051
p = 0.91
r=-0.62
p = 0.35

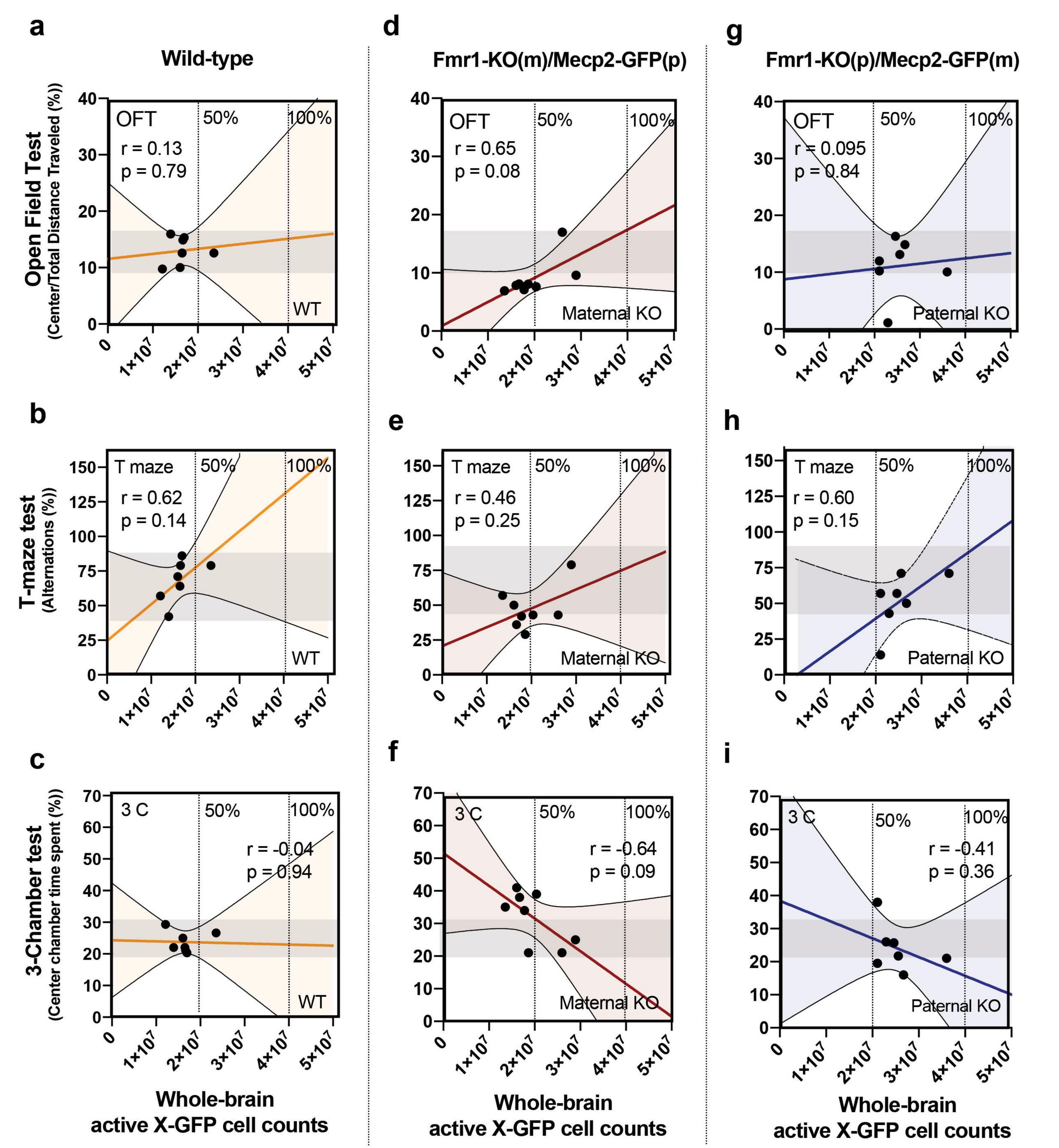
a
Wild-type
Open Field Test
(Center/Total Distance Traveled (%))
OFT
50%
100%
r = 0.13
p = 0.79
WT
d
Fmr1-KO(m)/Mecp2-GFP(p)
OFT
50%
100%
r = 0.65
p = 0.08
Maternal KO
g
Fmr1-KO(p)/Mecp2-GFP(m)
OFT
50%
100%
r = 0.095
p = 0.84
Paternal KO
b
T-maze test
(Alternations (%))
T maze
50%
100%
r = 0.62
p = 0.14
WT
e
T maze
50%
100%
r = 0.46
p = 0.25
Maternal KO
h
T maze
50%
100%
r = 0.60
p = 0.15
Paternal KO
c
3-Chamber test
(Center chamber time spent (%))
3 C
50%
100%
r = -0.04
p = 0.94
WT
f
3 C
50%
100%
r = -0.64
p = 0.09
Maternal KO
i
3 C
50%
100%
r = -0.41
p = 0.36
Paternal KO
Whole-brain
active X-GFP cell counts
Whole-brain
active X-GFP cell counts
Whole-brain
active X-GFP cell counts

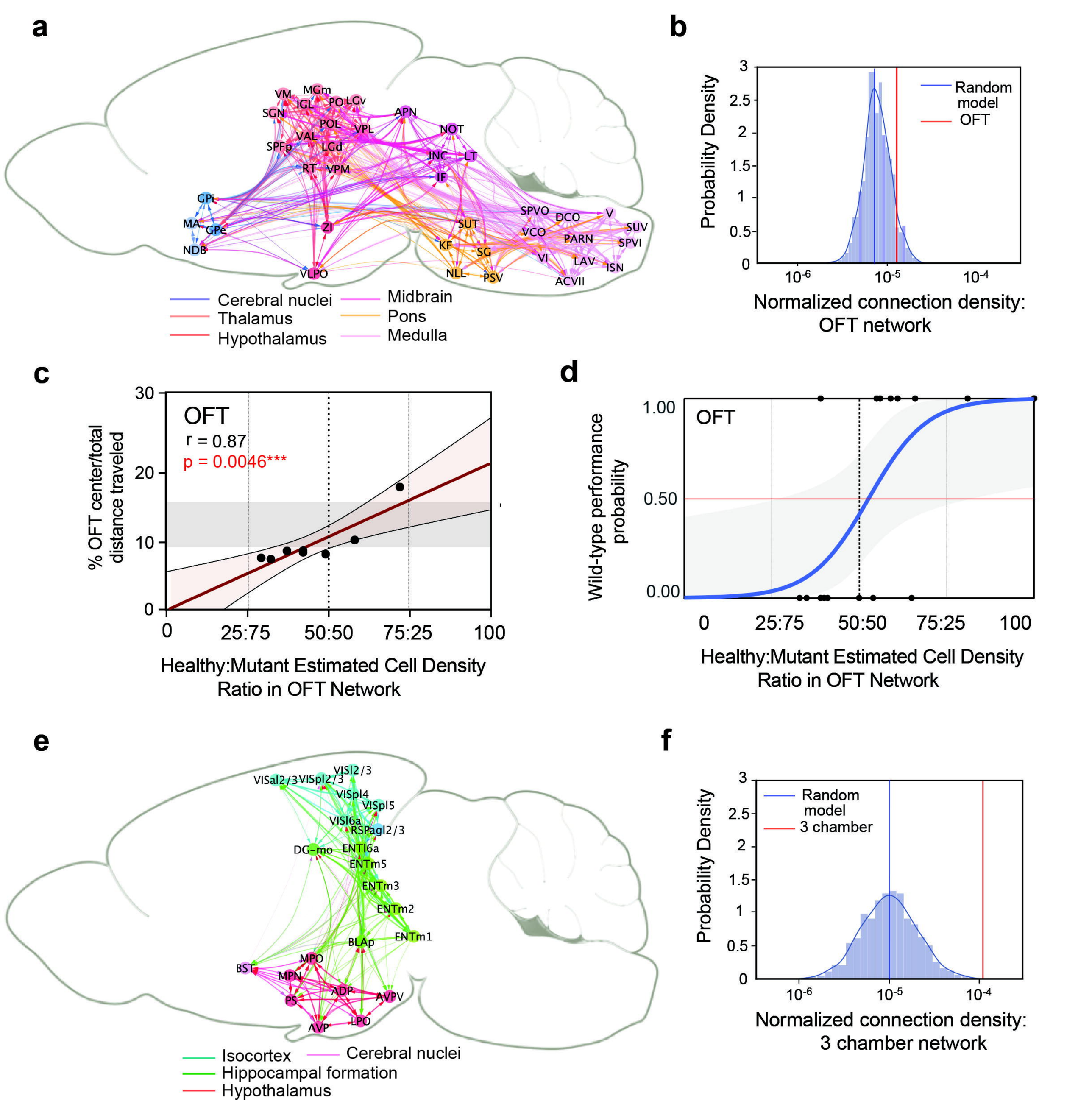
a
VM
MGm
IGL
PO
LGv
SGN
APN
POL
VPL
NOT
VAL
SPFp
LGd
INC
LT
RT
VPM
IF
GPi
MA
GPe
ZI
NDB
SUT
SPVO
DCO
V
SUV
VCO
PARN
SPVI
KF
SG
VI
LAV
ISN
VLPO
NLL
PSV
ACVII
Cerebral nuclei
Thalamus
Hypothalamus
Midbrain
Pons
Medulla
b
Probability Density
Random model
OFT
Normalized connection density: OFT network
c
OFT
r = 0.87
p = 0.0046***
% OFT center/total distance traveled
Healthy:Mutant Estimated Cell Density Ratio in OFT Network
d
OFT
Wild-type performance probability
Healthy:Mutant Estimated Cell Density Ratio in OFT Network
e
VISal2/3
VISpl2/3
VISl2/3
VISpl4
VISpl5
VISl6a
RSPagl2/3
DG-mo
ENTl6a
ENTm5
ENTm3
ENTm2
ENTm1
BLAp
MPO
BST
MPN
ADP
AVPV
PS
LPO
AVP
Isocortex
Hippocampal formation
Hypothalamus
Cerebral nuclei
f
Probability Density
Random model
3 chamber
Normalized connection density: 3 chamber network
g
3 chamber
r = -0.88
p = 0.0041***
% 3C center chamber time
Healthy:Mutant Estimated Cell Density Ratio in 3C Network
h
3 chamber
Wild-type performance probability
Healthy:Mutant Estimated Cell Density Ratio in 3C Network

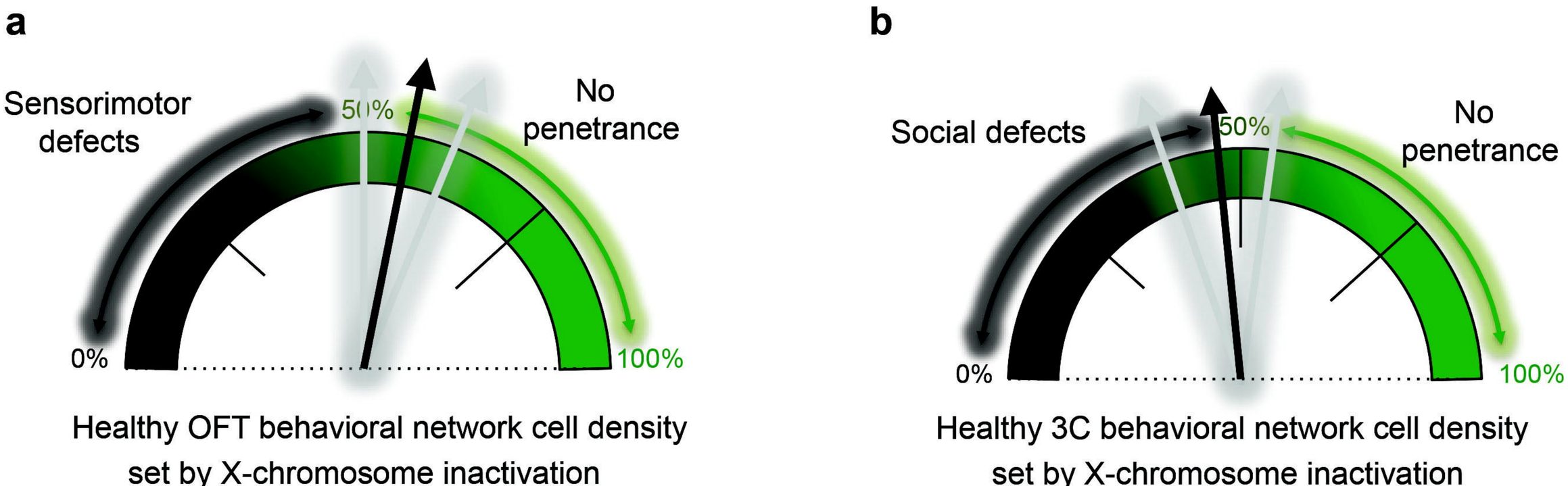
a
Sensorimotor defects
50%
No penetrance
0%
100%
Healthy OFT behavioral network cell density set by X-chromosome inactivation
b
Social defects
50%
No penetrance
0%
100%
Healthy 3C behavioral network cell density set by X-chromosome inactivation